Nanoscale

REVIEW

View Article Online
View Journal

Cite this: DOI: 10.1039/d4nr03493g

Recent advances in fundamental research on photon avalanches on the nanometre scale

Shradha Aggarwal [a,b]

In recent years, Photon Avalanche (PA) on the nanometre scale has emerged as a groundbreaking phenomenon, enabling the generation of high-energy photons with minimal pumping power due to its highly nonlinear optical dynamics. This review focuses on the advancement in photon-avalanching nanoparticles (ANPs), composed of lanthanide ion-doped inorganic matrices, which exhibit remarkable optical nonlinear response under low-power excitation. The objective of this article is to provide a comprehensive overview of the PA mechanism in nanoscale materials, with a specific focus on single-ANP systems. Key factors influencing the PA characteristics, such as excitation-power threshold, excited-state absorption, cross-relaxation process, dopant ion concentration, and temperature sensitivity are summarized. Furthermore, the review situates recent ANP research within the broader context of early studies on the PA mechanism observed in bulk crystals and optical fibers, highlighting the distinctive features and applications of ANPs. Notable applications discussed include single-particle and biological super-resolution imaging, deep-tissue imaging, luminescence thermometry, ANP-based lasers, optical data storage, and information security. The paper also addresses current challenges and limitations of ANPs in practical applications, proposing potential solutions and future research directions to facilitate their integration into real-world environments. This review aims to serve as a valuable resource for researchers seeking to advance the understanding and application of ANPs in various scientific and technological domains.

Received 26th August 2024,
Accepted 17th January 2025

DOI: 10.1039/d4nr03493g

rsc.li/nanoscale

1. Introduction

Through the PA phenomenon, ANPs exhibit highly nonlinear optical dynamics in response to even minute increments of pumping power.[1] PA in lanthanide-based materials is a nonlinear upconverting (UC) mechanism, in which a fractional increase in pumping power results in a significant increase in luminescence intensity – often 1000-fold or more. Such characteristics distinguish ANPs from the other lanthanide-doped luminescent or conventional upconverting materials, making them more sensitive to perturbations, both environmental or internal, during the chain reaction of cross-relaxation (CR) and excited-state absorption (ESA) that occurs during the avalanching processes.[2] Various applications, including single-particle tracking[3] and super-resolution imaging,[2–4] luminescence thermometry,[5,6] ANP-based lasers,[7] optical storage, and information security,[4] have been shown based on the high luminescence intensity of ANPs. ANPs are generally composed of inorganic crystalline host matrices such as $NaYF_4$, $NaGdF_4$, LaF_3, and CaF_3, *etc.*, doped with rare-earth lanthanide (Ln^{3+}) ions that work as absorber and emitter ions. Common Ln^{3+} dopants include ytterbium (Yb^{3+}), neodymium ion (Nd^{3+}), thulium (Tm^{3+}), erbium (Er^{3+}), and holmium (Ho^{3+}). These dopant ions are responsible for the PA effect by creating a positive feedback system analogous to the second-order phase transition of ferromagnetic spin systems.

In lanthanide-based PA, incident excitation is chosen so that its energy cannot be resonant with any ground-state absorption (GSA) transitions within the Ln^{3+} ions but is resonant with an ESA transition. This is accomplished, for example, by pumping the Tm^{3+}-based ANPs with a continuous wave (CW) near-infrared (NIR) laser at the wavelength of 1064 nm or 1450 nm. Under these conditions, a single (non-resonant) ground-state absorption (GSA) event initiates the chain reaction of ESA and CR events between Tm^{3+} ions. Within this chain reaction, a single excited Tm^{3+} ion absorbs an incident photon *via* ESA, putting it in a higher excited state. Then it can "donate" part of its energy to a neighboring Tm^{3+} ion *via* a CR process, placing both Tm^{3+} ions in an intermediate excited state prepared for ESA. These two Tm^{3+} ions' ESA leads to four Tm^{3+} ions' in the intermediate state *via* the subsequent CR process. This process can continue with multiple cycles, emitting multiple high-energy photon emission at 800 nm (approx)[2,3,8] Fig. 1.

Fluorescent organic molecular dyes and protein molecules (*e.g.* green fluorescent proteins (GFP), blue fluorescent protein

[a]IBS (Institute of Basic Science), 44919 Ulsan, Korea.
E-mail: aggarwalunist.in@unist.ac.kr
[b]Department of Chemistry, UNIST (Ulsan National Institute of Science and Technology), 44919 Ulsan, Korea

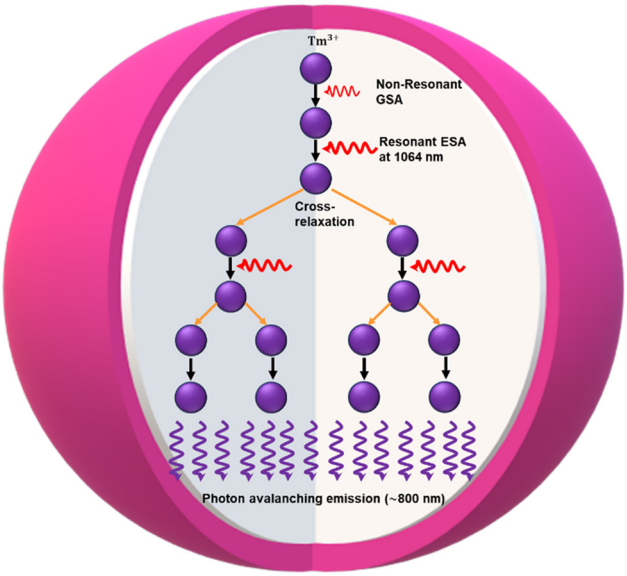

Fig. 1 Schematic illustration of PA mechanism in Tm^{3+}-doped core/shell avalanche nanoparticles under 1064 nm.

(BFP), or cyan fluorescent proteins) are most frequently used as photoluminescence probes in bioimaging, deep tissue imaging, and other biomedical applications, as they allow good compatibility with biological objects.[9–12] However, when exposed to radiation, many organic dye molecules exhibit photobleaching while continuously monitoring individual molecules and imaging subcellular organelles during real-time imaging.[13] In recent years, researchers have made great progress in designing luminescent nanoprobes that address the limitations of traditional fluorescent dyes and protein molecules. Specifically, many of these advances involve nanomaterial probes with distinct luminescence characteristics, such as perovskite quantum dots,[14] semiconductor quantum dots (QDs),[15,16] fluorescent nanodiamonds,[17] polymer dots,[18] Graphene nanodots (GNDs),[19,20] single-walled carbon nanotubes,[21,22] and copper–indium–selenium (CISE) nanotubes.[23] These nanoprobes are generally more resistant to photobleaching but still face stochastic photoblinking behavior, rendering them unsuitable for single-molecule-tracking. Additionally, the extent of their use in super-resolution microscopy is limited due to issues like toxicity and nonspecific binding to non-target areas.[13,16,18,19]

Conventional rare-earth upconversion nanoparticles (UCNPs) address most of these issues. They offer good biocompatibility, stability under prolonged radiation, and resistance to photobleaching and photoblinking. Additionally, they produce minimal background autofluorescence and have low bio-toxicity, making them superior to the above-mentioned probes. Nonetheless, their reliance on high-power excitation sources may limit their applicability in certain sensitive biological or environmental samples.[24,25] However, over the years, ANPs have made good luminescence markers because they frequently exhibit giant nonlinear responses in luminescence intensity and fast response times, enabling sensitive detection and imaging upon small NIR excitation intensity, particularly advantageous for heating-free bioimaging *in vitro*. Due to these unique spectral properties, ANPs are now being implemented as high-resolution optical probes for optical bioimaging, and other emerging photonic applications.[26] However, their utilization introduces complexity in measurement and interpretation, requiring sophisticated instrumentation and data analysis techniques. Additionally, ANPs are sensitive to environmental factors, potentially compromising measurement reliability as compared with traditional UCNPs.

Mechanistic research has dramatically improved the fundamental comprehension of Ln^{3+}-based UC over the past few decades. In general, several mechanisms have been described, including Excited state absorption (ESA),[27] Energy transfer upconversion (ETU),[28,29] Interfacial energy transfer (IET),[30] Cooperative energy transfer (CET),[31,32] as well as PA – the focus of this survey Fig. 2. PA is a unique phenomenon among these mechanisms because it generates a self-sustained process under a meager pump power due to the CR process. The PA mechanism is influenced by several interdependent factors that distinguish it from other nonlinear multiphoton processes. PA exhibits a distinct nonlinear power dependence, with a sharp excitation-power threshold or Photon avalanching threshold (I^{th}) beyond which the emission efficiency increases dramatically. This characteristic behavior is further supported by a characteristic S-shaped emission intensity power dependence and critical slowing down of rise times, with the rise time of the excited state population often extending well beyond the intermediate state's lifetime. An efficient PA process occurs in materials characterized by strong ESA and very weak GSA. This combination typically arises when the excitation radiation is resonant with ESA but not with the ground-state transition. The ratio of ESA to GSA cross-section $\left(\beta = \frac{\sigma_{ESA}}{\sigma_{GSA}}\right)$ should ideally exceed 10^4, ensuring stronger absorption from excited states. PA also relies on the electronic structure of the luminophore to enable "chain reaction", a process typically facilitated by CR, in which a pair of single excited state ions and ground state ions produce two intermediately excited ions by donating part of the excited state energy to a ground state ion. These ions can then absorb additional photons *via* ESA, enabling the looping cycle to repeat. With each iteration, the intermediate state population doubles, leading to a highly nonlinear amplification of light emitted by that state and other associated states. The dopant ion concentration also plays a pivotal role. Optimal spacing is required to maximize energy transfer while avoiding quenching from excessive proximity. Additionally, temperature sensitivity impacts PA efficiency: higher temperature can enhance energy transfer but may also increase phonon-mediated losses.[1,8,33–35] Together, these factors synergistically define the PA mechanism and differentiate it from conventional energy-transfer upconversion[36] or energy-looping processes.[37]

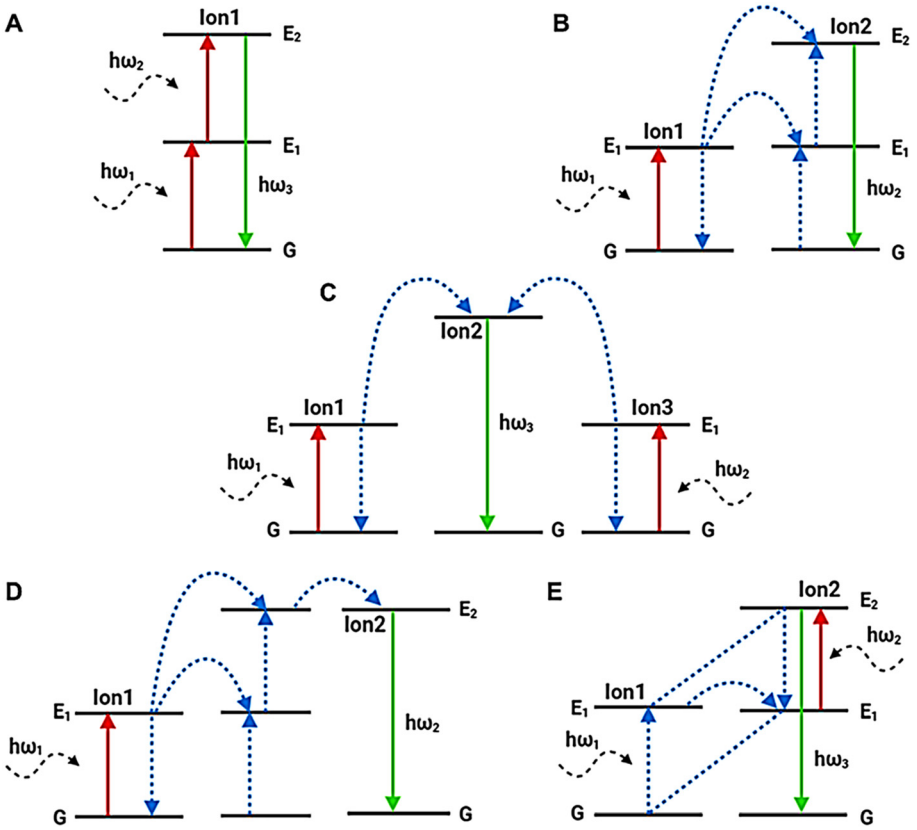

Fig. 2 Schematic illustration of the fundamental UC mechanism in lanthanide ions. (A) Excited state absorption (ESA). (B) Energy transfer UC (ETU). (C) Cooperative energy transfer (CET). (D) Interfacial energy transfer (IET). (E) Photon avalanche (PA).

The initial discovery of PA was first observed in 1979 by Jay S. Chivian in lanthanide-doped bulk crystal of $LaCl_3$:Pr^{3+} or $LaBr_3$:Pr^{3+} to detect medium infrared photons by signal radiation around 4.5 μm. These photons played a crucial role in populating the intermediate $^3H_5$ level within the crystals. Subsequently, efficient photoexcitation was achieved using a CW green laser source, facilitating the transition from the $^3H_5 \rightarrow {}^3P_1$ ESA. When this pumping source exceeds a certain threshold value, Pr^{3+} fluorescence from the $^3P_1$ or $^3P_0$ realization is enhanced by orders of magnitude.[38] Its discovery accelerated the development of more lanthanide-based PA bulk materials in the context of UC lasing and quantum counters.[39,40] Unfortunately, until very recently, this discovery of PA in bulk material did not translate to nanomaterials due to increased complexity and losses present in nanostructured systems.

This review delves into recent advancements in fundamental and applied research on PA at the nanoscale, focusing on the unique properties and mechanisms of ANPs. By exploring state-of-the-art studies, we aim to provide a comprehensive understanding of the design, control, and functional optimization of ANPs. To contextualize these developments, the review compares nanoscale PA phenomena with earlier observations in bulk crystals and optical glass fibers, highlighting the distinctive features and advantages of ANPs in modern applications. The objective of this review is to guide future research by offering a detailed analysis of the mechanisms driving PA in ANPs, emphasizing factors like energy transfer processes, dopant concentration, and environmental influences. Additionally, we examine the potential of ANPs to push the boundaries of nanotechnology through cutting-edge applications, including super-resolution imaging, deep-tissue imaging, luminescence thermometry, ANP-based lasers, optical data storage, and information security. By addressing current challenges and proposing strategies for overcoming limitations, this review aims to inspire innovative approaches for the intelligent design and real-world implementation of ANPs. The overall organizational theme of the review is shown in Fig. 3.

2. Photon avalanche historical evaluation from bulk crystals to nanoparticles

2.1. Photon avalanche in bulk crystals

PA was initially observed using crystals doped with Pr^{3+} ions in infrared quantum counters. These crystals, specifically $LaCl_3$ or $LaBr_3$, were doped with Pr^{3+} ions into their lattice structure and subjected to laser-pump radiation tuned precisely to the

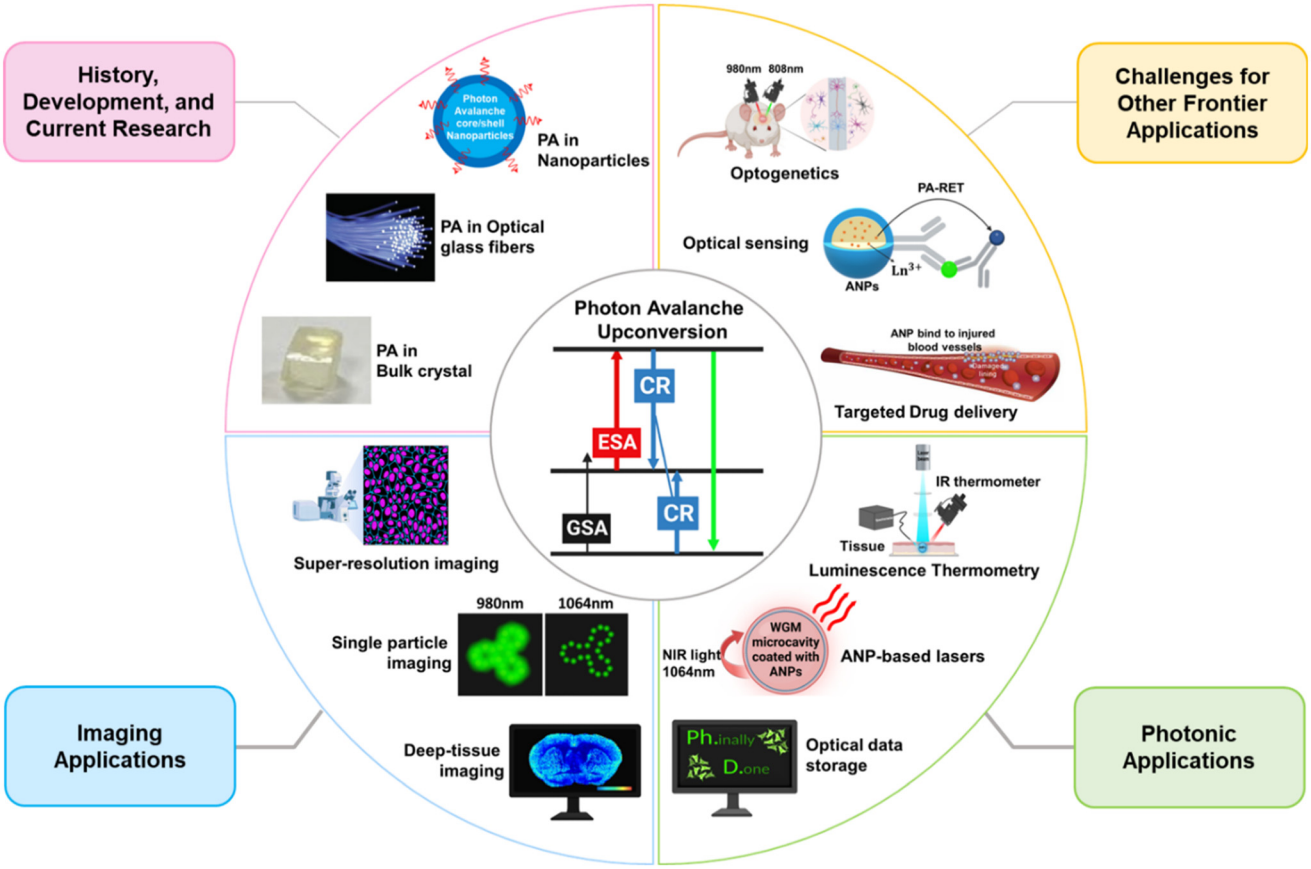

Fig. 3 Schematic representation of photon avalanche (PA) upconversion and its diverse developments, as explored in this article.

absorption frequency of the excited state transition ($^3H_5 \rightarrow {}^3P_1$). When the intensity of this laser radiation slightly exceeded a specific critical threshold, an extraordinary phenomenon occurred: the fluorescence emitted by the Pr^{3+} ions increased dramatically. This enhancement in fluorescence led to a noticeable decrease in the intensity of the photo-excitation source as it propagated through the crystal. This remarkable behavior was attributed to an efficient resonant energy transfer mechanism involving the $^3H_6$, $^3H_5$, and $^3H_4$ infrared states of Pr^{3+} ions. The UC process facilitated by these states played a pivotal role in achieving a large population of excited states, a condition crucial for the quantum counting process.[38] The significant increase in fluorescence intensity was a direct result of this resonant energy transfer, which amplified the PA effect and made it highly efficient. This discovery marked a groundbreaking advancement in the understanding of PA phenomena. It was the first recorded instance of such a process and served as a foundation for developing other lanthanide-based quantum counter materials.

Building on this initial work with Pr^{3+}-doped crystals, subsequent research extended the concept to other lanthanides, such as Sm^{3+}, and Nd^{3+}, which exhibited similar PA effects.[39,40] These materials found applications in solid-state laser systems, particularly under cryogenic conditions at temperatures of ≤40 K. This pioneering research not only elucidated the mechanisms behind PA but also spurred innovation in the field of quantum counter materials and infrared laser technology. We have collected comprehensive data on the PA effect in "bulk" crystals, summarized in Table 1. The PA mechanism presents an intriguing method to pump an upconverting laser at a relatively low pumping irradiance due to the population inversion it exhibits. This unique feature has spurred the study of PA in various lanthanide-doped bulk crystals.[33,34,41,42] For instance, Brenier *et al.* described a looping mechanism observed in Er^{3+}-doped $YAlO_3$ oxide crystal, which emitted green at 550 nm ($^2P_{3/2} \rightarrow {}^4I_{11/2}$) and blue emission at 475 nm ($^4S_{3/2} \rightarrow {}^4I_{15/2}$) when excited by CV laser radiation in the 690–810 nm range at room temperature.[43] This observation demonstrated the potential of Er^{3+}-doped crystals for PA-based upconversion, as the fluorescence intensity significantly increased once the excitation intensity surpassed a specific threshold. Hebert *et al.* further contributed to the study of PA effects by demonstrating the generation of intense blue UC emission at 483 nm ($^1G_4 \rightarrow {}^3H_6$) in a 1.8% Tm-doped $LiYF_4$ fluoride crystal.[44] This emission was induced by a single red-dye laser operating at 628.6 nm which resonated only with absorption from a metastable state, but not from the ground state. The avalanche absorption pumping scheme proved to be effective even at cryogenic temperatures, down to 160 K, showcasing the versatility of PA in various temperature regimes.

Table 1 Survey report of the PA-like behavior in "Bulk" Crystals since 1949

Host crystal	Dopant ions	Excitation	Emission	Excitation power threshold	Transition states	Temperature	Ref.
$Y_3Al_5O_{12}$	5% Tm^{3+}	617 nm	Blue emission (486 nm)	1.3	$^1G_4 \rightarrow {}^3H_6$	35 K	33
$LaCl_3$ or $LaBr_3$	3–4.8% Pr^{3+}	4500 + 529	Red emission	1.2–12.2 W cm^{-2}	$^3P_0 \rightarrow {}^3H_6$ $^3P_1 \rightarrow {}^3F_2$	20–300 K	38
$LaBr_3$	1.05% Sm^{3+}	IR + 593.2 nm	Red emission (644 nm)	—	—	4.2 K	39
$CeCl_3$	1% Nd^{3+}	Red	—	135 mW and 40 mW	—	4.2–60 K	40
$LiYF_4$	1% Nd^{3+}	603.6 nm	Blue emission (413 nm)	~50 kW cm^{-2}	$^2P_{3/2} \rightarrow {}^4I_{11/2}$	30 K	42
$YAlO_3$	1.5% Er^{3+}	690 nm–810 nm	Green and blue emissions (550 nm, 405 nm, and 475 nm)	—	$^4S_{3/2} \rightarrow {}^4I_{15/2}$ $^2P_{3/2} \rightarrow {}^4I_{13/2}$ $^2P_{3/2} \rightarrow {}^4I_{11/2}$	Room	43
$YALO_3$	2% Tm^{3+}	649.5 nm	Blue emission (475.6 nm)	1 kW cm^2	$^1G_4 \rightarrow {}^3H_6$	Room	44
$LiYF_4$	1.8% Tm^{3+}	628.6 nm (red-dye laser)	Blue emission (483 nm)	—	$^1G_4 \rightarrow {}^3H_6$	160 K	44
$Cs_2NaGdCl_6$	10% Tm^{3+}	650 nm	Blue emission (480 nm)	9 kW cm^2	$^1G_4 \rightarrow {}^3H_6$	Room	45
$Cs_2NaGdCl_6$	1% Tm^{3+}, 10% Ho^{3+}	785 nm	Blue and red emission (483 nm, 658 nm, and 701 nm)		$^1G_4 \rightarrow {}^3H_6$ $^1G_4 \rightarrow {}^3F_4$ $^3F_3 \rightarrow {}^3H_6$	Room	46
$Cs_2NaGdCl_6$	10% Tm^{3+}, 10% Ho^{3+}	785 nm	Blue, green, yellow, and red emission (492 nm, 593 nm, 588 nm, and 657 nm)		$^5F_3 \rightarrow {}^5I_8$ $^5S_2 \rightarrow {}^5I_8$ $^5G_4 \rightarrow {}^5I_6$ $^5F_5 \rightarrow {}^5I_8$	Room	46
YAG	5% Ho^{3+}	594 nm	Green emission (545 nm)	90 mW	$^5S_2 \rightarrow {}^5I_8$	300 K	48
YAP	5% Ho^{3+}	586 nm		110 mW			
YLF	1% Ho^3	580 nm		164 mW			
$LaCl_3$	3–7% Pr^{3+}	677 nm	644 nm	~2.3 kW cm^{-2}	$^3P_0 \rightarrow {}^3F_2$	$80 < T < 210$	49
YAG	3% Tm^{3+}	638 nm	Blue emission (486.2 nm)	100 mW	$^1G_4 \rightarrow {}^3H_6$	Cryogenic temp.	50
LaF_3	1% Tm^{3+}	635.2 nm	Blue emission (480 nm)	100 mW	$^1G_4 \rightarrow {}^3H_6$	77 K	51
$LiYF_4$	5% Er^{3+}	579 nm	Green emission (550 nm)	37 mW	$^4S_{3/2} \rightarrow {}^4I_{15/2}$	Room	52
YLF	3% Tm^{3+}	477.4 and 483 nm (pump–probe)	477 nm	~50 mW	$^1G_4 \rightarrow {}^3H_6$	160 K	53
$LiKYF_5$	5% Tm^{3+}, 0.1% Er^{3+}	648 nm	Blue emission (450 nm)	~1 kW cm^2	$^1D_2 \rightarrow {}^3F_4$	77 K	54
β-Na $(Y_{1.5}Na_{0.5})F_6$	0.5% Ho^{3+}	980 nm	Green emission (540 nm)	370 mW	$^5S_2 \rightarrow {}^5I_8$	Room	55

In conventional studies, photon avalanching in Tm^{3+}-doped crystals, typically achieved by pumping with Infrared (IR) or dye laser, has predominantly been observed at room temperature. For instance, in the case of the elpasolite crystal $Cs_2NaGdCl_6$ doped with 10% Tm^{3+} ions, intense blue luminescence near 450 nm and/or 480 nm was generated under 650 nm laser excitation at room temperature. This emission was attributed to the PA pumping process.[45] Further investigation on the same crystal samples including singly doped with 1% Tm^{3+} and 10% Ho^{3+}, and co-doped with 10% Tm^{3+} and 10% Ho^{3+}, revealed interesting emission bands.[46] Under 785 nm excitation, the 1% Tm^{3+} single-doped sample exhibited three avalanche emission bands near 483 nm (blue), 658 nm (red), and 701 nm (infrared) assigned to be $^1G_4 \rightarrow {}^3H_6$, $^1G_4 \rightarrow {}^3F_4$ and $^3F_3 \rightarrow {}^3H_6$ states, respectively. The 10% Tm^{3+} co-doped sample, on the other hand, exhibited four strong emissions bands near 492 nm (blue), 593 nm (green), 588 nm (yellow), and 657 nm (red) attributed to various transitions of Ho^{3+} ions, namely $^5F_3 \rightarrow {}^5I_8$, $^5S_2 \rightarrow {}^5I_8$, $^5G_4 \rightarrow {}^5I_6$, and $^5F_5 \rightarrow {}^5I_8$.

In contrast, Ni *et al.* observed the abrupt onset of fluorescence and avalanche absorption dynamics at 649.5 nm in a 2% Tm^{3+}:$YAlO_3$ crystal at room temperature.[47] The laser source, which was not resonant with any GSA, induced ions to transition to excited states through short-range interactions between excited ions and neighboring ground-state ions. This process led to increased absorption and the emission of strong blue UC fluorescence at 475.6 nm ($^1G_4 \rightarrow {}^3H_6$) transition above a sharp threshold intensity. Malinowski *et al.* also explored avalanche UC at room temperature in Ho^{3+} ion-doped oxide and fluoride crystals including YAG, YLF, and, YAP crystals, which emitted strong green fluorescence at 545 nm corresponding to the $^5S_2 \rightarrow {}^5I_8$ transition of Ho^{3+} ions under CW orange light excitation in the 580–590 nm spectral range.[48]

The collective findings from these studies on avalanche behavior in "bulk" crystals have sparked the development of solid-state lasers for a range of practical applications, such as optical data storage, full-color displays, and medical instrumentation. However, while bulk crystals offer exciting potential, their use is somewhat limited for certain applications, particularly in the biomedical field. One significant drawback of using bulk crystals in this context is their size. Larger crystals can be prone to failure due to mechanical stress or other factors, and they may not be as suitable for implantation or use in devices that require biocompatibility. This challenge has motivated further research into the development of smaller, more adaptable crystal-based systems, or alternatives

such as nanomaterials, which could overcome these limitations and better serve the needs of biomedical applications.

2.2. Photon avalanche in optical glass

Following the extensive studies on bulk crystals, researchers turned their attention to halide-based glass fibers as a promising alternative for light emission applications. These materials were found to possess low-vibrational phonon energies, which significantly enhanced their efficiency in facilitating photon upconversion processes compared with bulk crystal materials. The unique properties of halide-based glass fibers, such as their flexibility, high optical quality, and ability to guide light over long distances, made them a favorable choice for exploring avalanche behaviors in a fiber geometry. By doping several lanthanide ions into different types of glass fibers, scientists were able to successfully replicate and enhance the PA effect observed in bulk crystals. These fibers not only exhibited efficient upconversion emission but also demonstrated the capability to sustain avalanche processes up to room temperature, a critical requirement for practical applications.

For instance, Auzel *et al.* reported a significant demonstration of PA emission in a fluoride-based glass fiber composed of 4% Er^{3+}-doped ZBLAN.[56] Under photoexcitation with a laser tuned to 579.2 nm, this material exhibited a strong green PA emission centered at 550 nm, corresponding to the $^4S_{3/2} \rightarrow {}^4I_{15/2}$ transition of Er^{3+} ions. Notably, the emission showed a steep threshold intensity at approximately 60 kW cm^{-2}, highlighting the non-linear and highly efficient nature of the avalanche process in this system. Similarly, Martin *et al.* explored the PA effect in 2.5% Tm^{3+}-doped fluoride glass fiber.[57] When subjected to red laser excitation at 650.5 nm, this material emitted intense blue emission at two distinct wavelengths: 445 nm ($^1D_2 \rightarrow {}^3F_4$) and 475 nm ($^1G_4 \rightarrow {}^3H_6$). The results demonstrated the potential of fluoride glasses for achieving efficient PA-driven upconversion in the blue spectral region. Further studies by Lahoz *et al.* investigated PA emission in a 2.5% Ho^{3+}-doped fluoroindate glass.[58] This material, when excited with a laser at 747 nm, emitted a vivid green light at 545 nm corresponding to the combined $^5S_2$,$^5F_4 \rightarrow {}^5I_8$ transitions of Ho^{3+} ions.

M. F. Joubert *et al.* also observed intense blue emission at 481 nm in 3% Tm^{3+}-doped BIGaZYTZr fluoride glass from the $^1G_4$ and $^1D_2$ levels, under continuous wave excitation at 648.7 nm infrared.[59] The dynamics and power dependencies of both $^1G_4$ and $^1D_2$ fluorescence under 648.7 nm excitation revealed a PA mechanism. At higher concentration CR energy transfer and excited state absorption mechanisms compete to feed the $^1G_4$ and $^1D_2$ levels. Guy *et al.* reported the PA effect in a 3.2 wt% Tm^{3+}-doped ZBLAN optical fiber at room temperature.[60] Pumping at 630–650 nm, which is not resonant with the ground-state absorption, resulted in intense blue emissions at 450 nm ($^1D_2 \rightarrow {}^3F_4$) and 480 nm ($^1G_4 \rightarrow {}^3H_6$). It was established that the primary mechanism involves excited-state CR *via* the $^3H_6$ ground state of Tm^{3+}. A brief comprehensive report of optical glass fiber in which the PA effect has been observed is given in Table 2. The PA effect was also observed in 2.5% of Ho^{3+}-doped ZBLAN optical glass fiber under non-resonant excitation at 980 nm laser,[61] and strong green emis-

Table 2 Survey report of PA-like behavior in "Optical glass fibers" since 1993

Glass fiber	Dopant ions	Excitation	Emission	Transition states	Excitation power threshold	Temperature	Ref.
ZBLAN	1% Ho^{3+}	581 nm	Green emission (545 nm)	$^5S_2{}^5F_4 \rightarrow {}^5I_8$	124 mW	Room	48
ZBLAN	4% Er^{3+}	579.2 nm	Green emission (550 nm)	$^4S_{3/2} \rightarrow {}^4I_{15/2}$	60 kW cm^{-2}	Room	56
Fluoroindate glass	2.5% Tm^{3+}	650.5 nm	Blue emission (445 nm and 475 nm)	$^1D_2 \rightarrow {}^3F_4$ $^1G_4 \rightarrow {}^3H_6$	—	Room	57
Fluoroindate glass	2.5 Ho^{3+}	747 nm	Green emission (545 nm)	$^5S_2{}^5F_4 \rightarrow {}^5I_8$	68 mW	Room	58
BIGaZYTZr (BIG)	3% Tm^{3+}	649 nm	Blue emission (481 nm)	$^1D_2 \rightarrow {}^3F_4$ $^1G_4 \rightarrow {}^3H_6$	80 mW	4.2–300 K	59
ZBLAN	3–2% Tm^{3+}	630–650 nm	Blue emission (450 nm and 480 nm)	$^1D_2 \rightarrow {}^3F_4$ $^1G_4 \rightarrow {}^3H_6$	>50 mW	Room	60
ZBLAN	2.5% Ho^{3+}	980 nm	Green and red emission (540 nm, 652 nm and 766 nm)	$^5S_2{}^5F_4 \rightarrow {}^5I_8$ $^5F_5 \rightarrow {}^5I_8$ $^5S_2{}^5F_4 \rightarrow {}^5I_7$	100 mW	—	61
SiO_2 fiber	9–13% Pr^{3+}	670 nm	Blue and green emission (490 nm and 560 nm)	$^3P_0 \rightarrow {}^3H_4$ $^3P_0 \rightarrow {}^3H_6$	<0.5 W cm^{-2}	—-	62
ZBLAN	Pr^{3+}	780–880 nm	Red, orange, green, and blue emission (635 nm, 615 nm, 520 nm, and 493 nm)	$^3P_0 \rightarrow {}^3F_2$ $^3P_0 \rightarrow {}^3F_2$ $^3P_1 \rightarrow {}^3H_5$ $^3P_0 \rightarrow {}^3H_4$	42 mW 29 mW 21 mW 60 mW	Room	63
ZBLAN glass and fiber	3% Er^{3+}	690–700 nm	Green emission (550 nm)	$^4S_{3/2} \rightarrow {}^4I_{15/2}$	100 mW 4 mW	Room	64
ZBLAN	3% Er^{3+}	579 nm	Green emission (550 nm)	$^4S_{3/2} \rightarrow {}^4I_{15/2}$	5 mW	Room	64
ZBLAN	5% Ho^{3+}	585 nm	Green emission (545 nm)	$^5S_2{}^5F_4 \rightarrow {}^5I_8$	180 mW	77 K	65
ZBLAN	1% Ho^{3+} 5% Tm^{3+}	585 nm	Green emission (545 nm)	$^5S_2{}^5F_4 \rightarrow {}^5I_8$	180 mW	77 K	66
Fluorozinconate glass ZBYA	2.5% Ho^{3+}	750 nm and 840 nm	Green emission (545 nm)	$^5S_2{}^5F_4 \rightarrow {}^5I_8$	25 mW 36 mW	Room	67

sion at 540 nm ($^5S_2$,$^5F_4 \rightarrow {}^5I_8$) was detected, accompanied by two other longer wavelength bands at 652 nm ($^5F_5 \rightarrow {}^5I_8$) and 766 nm ($^5S_2$,$^5F_4 \rightarrow {}^5I_7$). On the other hand, Gomes *et al.* obtained the PA effect in 300–400 ppm of Pr^{3+}-doped silica-based optical fiber[62] under CW visible laser diode at 670 nm, which exhibited emission in the blue-to-green region at 490 nm and 560 nm corresponding to $^3P_0 \rightarrow {}^3H_4$ and $^3P_0 \rightarrow {}^3H_6$ transition with threshold power density <0.5 W cm^{-2}.

PA optical fibers have become highly valued in laser technology for their efficient light transmission and flexibility, making them essential in fabricating solid-state lasers and directing laser light to various systems. Their ability to deliver precise and efficient optical performance has made them a cornerstone of advanced photonic applications. However, these fibers also face notable limitations. Their design and manufacturing processes are highly complex and costly due to the precise doping and material requirements. Additionally, PA fibers have a limited operating range, often optimized for specific wavelengths, reducing their versatility. The avalanche process can generate high noise levels, complicating their use in systems demanding stable outputs. Moreover, their photon-detection efficiency is often insufficient for applications requiring high sensitivity, such as low-light imaging or quantum optics. These challenges must be addressed to expand the utility of PA optical fibers in broader technological fields.

2.3. Photon avalanche in lanthanide ion-doped nanoparticles

The observation of the PA effect at the nanoscale has shown promising results, particularly for practical applications when compared with bulk crystals or fragile optical glass.[68] This is due to the unique properties offered by ANPs including the following.

Size and surface area. ANPs typically have a high surface-to-volume ratio due to their nanoscale dimensions. The small size also offers advantages in terms of dispersibility and bioavailability in biological systems for applications in biomedicine.[69]

Tunability. Nanomaterials provide a greater degree of tunability concerning size, shape, and surface properties, offering flexibility for customization and optimization tailored to specific applications compared with bulk crystals.[69]

Enhanced efficiency. The smaller dimensions of nanoparticles can lead to enhanced efficiency in PA processes due to energy confinement, which is particularly beneficial for practical implementation.[2]

Scalability and manufacturing. Nanoparticle synthesis techniques have advanced significantly, enabling scalable and cost-effective production of PA nanomaterials that can be fabricated utilizing solution-based methods, like sol–gel-based formation and/or hydrothermal synthesis, which can be more amenable for large-scale manufacturing compared with the growth of bulk crystals for the fabrication of complex optical fibers.[70] However, it is important to note that observing photon avalanching at the nanoscale is challenging because of the strict preconditions appropriate to establish a cascade system. Researchers are actively exploring and investigating PA in nanoparticles to optimize efficiency and unlock new opportunities for cutting-edge applications, including nanophotonics, biological imaging, and information storage. In recent years, several reports have highlighted the advancements in ANPs. These studies have demonstrated improved efficiency, novel synthetic approaches, and expanded applications of PA nanomaterials. By harnessing the unique properties of ANPs, researchers are paving the way for transformative advancements in photonics and related fields.

Using theoretical modeling, Bednarkiewicz *et al.* proposed a PA behavior in Nd^{3+}-doped nanoparticles under 1064 nm photoexcitation.[26] This wavelength corresponds to the ESA $^4I_{11/2} \rightarrow {}^4F_{3/2}$ transition, where the ESA cross-section (σ_{ESA}) is significantly larger than the GSA cross-section (σ_{GSA}), favoring the population of the excited state. As the excitation intensity increases, energy transfer between neighboring Nd^{3+} ions through the CR process (W_{CR}) leads to a feedback loop that significantly enhances the population of the intermediate $^4I_{11/2}$ state. This looping mechanism amplifies the emission intensity in a highly nonlinear manner, which is crucial for PA behavior. Although non-radiative losses can reduce the efficiency of this process, these losses are accounted for in rate equation models by incorporating the non-radiative decay pathways of the $^4I_{11/2}$ state Fig. 4(A and B). Based on *in silico* studies of these PA-dependent factors and excitation intensities, researchers achieved an "S"-shaped emission response above a critical PA threshold ($P_{IN} > P_{TH}$) and below saturation regime ($P_{IN} < P_S$) – which is characteristic of PA behavior Fig. 4(C). This sharp nonlinearity enables the exploitation of ANPs for photon-avalanche single excitation beam sub-resolution imaging (PASSI) techniques as luminescent labels and enhances optical resolution up to the sub-nanometre.

As per recent reports, researchers have revealed experimental studies in which highly doped nanocrystals can exhibit a PA behavior, where specific energy levels are populated through positive feedback under certain excitation conditions. One significant advancement in this field is the use of Tm^{3+}-doped nanoparticles that display PA-like behavior at room temperature. These nanoparticles show exceptionally strong nonlinear optical responses and have been successfully applied in sub-diffraction imaging techniques within the NIR biological window. In 2021, Lee *et al.* reported a significant advancement in this field by achieving the PA effect at room temperature in core/shell nanoparticles doped with 8% Tm^{3+} ions[2] (Fig. 5A). These nanoparticles were excited with a CW laser operating at 1450 nm, a wavelength resonant with the ESA transition between the $^3F_4$ and $^3H_4$ energy levels of Tm^{3+}. The experimental report confirmed all the hallmark features of PA, including clear PA threshold, slowdown of the excited-state population rise times at threshold, and a stronger power-laser-induced ESA, which was more than 10^4 times greater compared with the GSA. Above the avalanching threshold, a larger nonlinear response exhibited up to the 26th power of the pump intensity, and emission observed at 800 nm Fig. 5(B and C) due to induced positive optical feedback in each nanoparticle enabled the experimental realization of photon-ava-

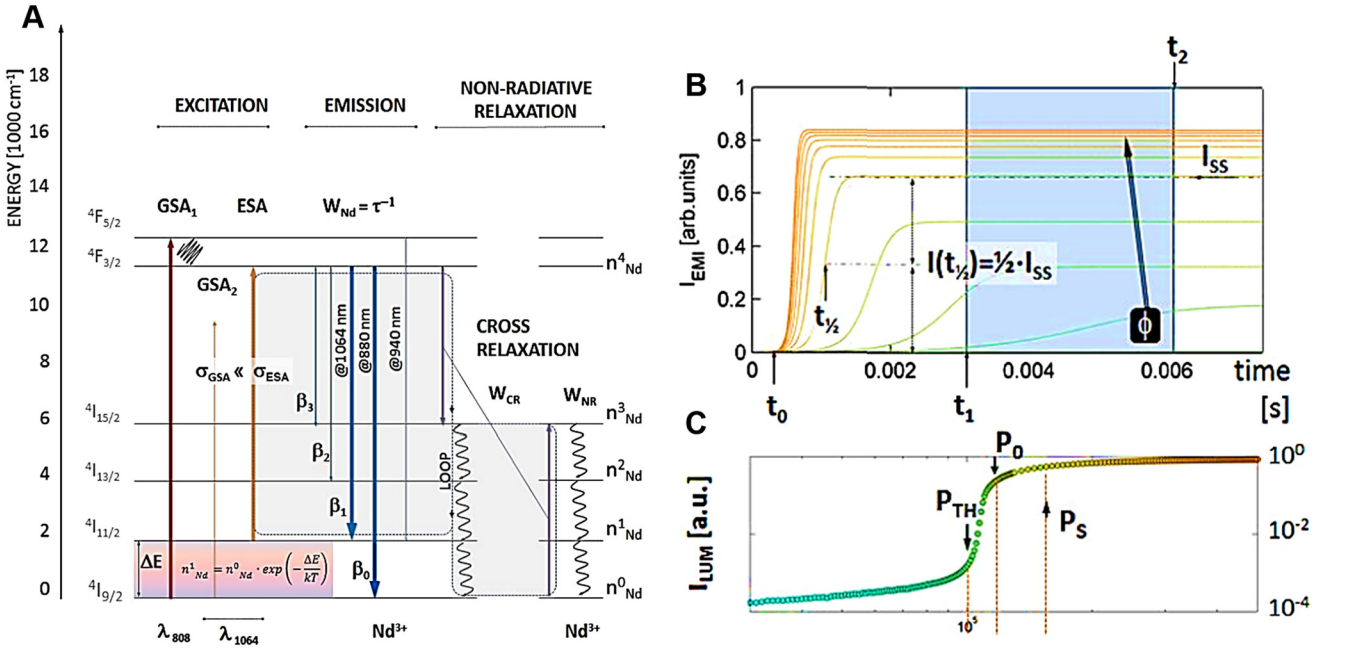

Fig. 4 PA in Nd^{3+}-doped nanoparticles. (A) Energy-level diagram of Nd^{3+} ions showing under 1064 nm photoexcitation resonant with ESA, radiative emission (W_{Nd}) from $^4F_{3/2}$ state and CR (W_{CR}) leading repeated population of the $^4I_{11/2}$ state. (B) The power-dependent PA emission profiles, ranging from green to orange, were simulated using a rate equation model for Nd^{3+} ions. Key parameters like steady-state intensity (I_{ss}), half-rise time ($t_{1/2}$), and time points (t_0, t_1, t_2) were used to quantify the PA behavior. (C) The steady-state PA emission ($I_{ss} = I_{LUM}(t \to \infty)$). I_{LUM} represents luminescence intensity. Reproduced with permission from ref. 26. Copyright 2019, The Royal Society of Chemistry.

lanche single-beam super-resolution imaging[26] with sub-70 nm spatial resolution, far beyond the diffraction limit of conventional optical microscopy. The simplicity of this approach coupled with the exceptional photostability of the Tm^{3+}-doped ANPs highlighted their suitability for applications in sub-diffraction imaging,[4,26] optical sensing,[5,6] and environmental monitoring[7] within the NIR biological window.

Building upon this foundation, Liang *et al.* developed an advanced PA system based on a core/shell architecture doped with Yb^{3+} and Pr^{3+} ions.[3] This system leveraged the ESA transition in Pr^{3+} ($^1G_4 \rightarrow {}^3P_1$), triggered by a CW laser operating at 852 nm, which was strategically chosen to be off-resonant with the GSA transition of both Yb^{3+} and Pr^{3+} Fig. 5(D). The resulting feedback loop between ESA and energy transfer facilitated a robust PA mechanism within the core of the nanoparticles. This study demonstrated a nonlinear optical response with a 26th-order dependence on the excitation power, with a clearly defined PA threshold of about 60 kW cm^{-2} Fig. 5(E). To further enhance the optical response, the authors synthesized Ho^{3+} and Tm^{3+}-doped multi-layer shells around the core. The Migrating PA (MPA) mechanism allowed the avalanche process initiated in the core to propagate outward, inducing a nonlinear response in the Ho^{3+} and Tm^{3+} ions located in the shell layer. Remarkably, the Tm^{3+} ions in the outermost shell exhibited a 46th-order nonlinear response of 452 nm blue emission with a PA threshold of 120 kW cm^{-2} Fig. 5(F and G). This cascading multiplicative effect significantly amplified the optical nonlinearity, facilitating super-resolution imaging with a lateral resolution of ~62 nm using a single low-power CW laser.

In a subsequent study, Zhan *et al.* achieved nanoscale PA effects by introducing a Tandem PA mechanism utilizing IET across a multilayered nanostructure.[71] They synthesized $NaYF_4$:8%Tm^{3+} core/shell nanoparticles, where the avalanche core acted as a PA nano-engine, triggering high-order nonlinear responses in shell emitters. This approach achieved a 41st-order nonlinearity at a low PA threshold of 7.1 kW cm^{-2} and a 475 nm blue emission avalanche from Tm^{3+} under a single 1064 nm excitation, highlighting the potential of IET in enhancing optical nonlinearity.

As per recent research on ANPs, Zhan *et al.* introduced a novel mechanism called energy relay-mediated photon-avalanche (enrePA), which further enhanced the PA process by incorporating a relay system within the nanoparticle architecture.[72] Unlike the traditional PA mechanism, in this system, Yb^{3+} ions located in the outer shell captured the avalanching energy from the avalanched core through an IET process ($^3H_4 \rightarrow {}^2F_{5/2}$), effectively relaying the energy of Tm^{3+} ions and populating them into higher energy states. This innovative energy relay mechanism enabled a giant optical nonlinear response up to the 60th order from the Tm^{3+} ions, leading to intense blue emission at 452 nm under a single CW 1064 nm irradiation (45.6 kW cm^{-2}) Fig. 6(A and B). To further expand this concept, the research team incorporated Gd^{3+}-based systems, allowing the activation of additional lanthanide emitters, such as Tb^{3+}, Eu^{3+}, Dy^{3+}, and Nd^{3+}, resulting in nonlinear

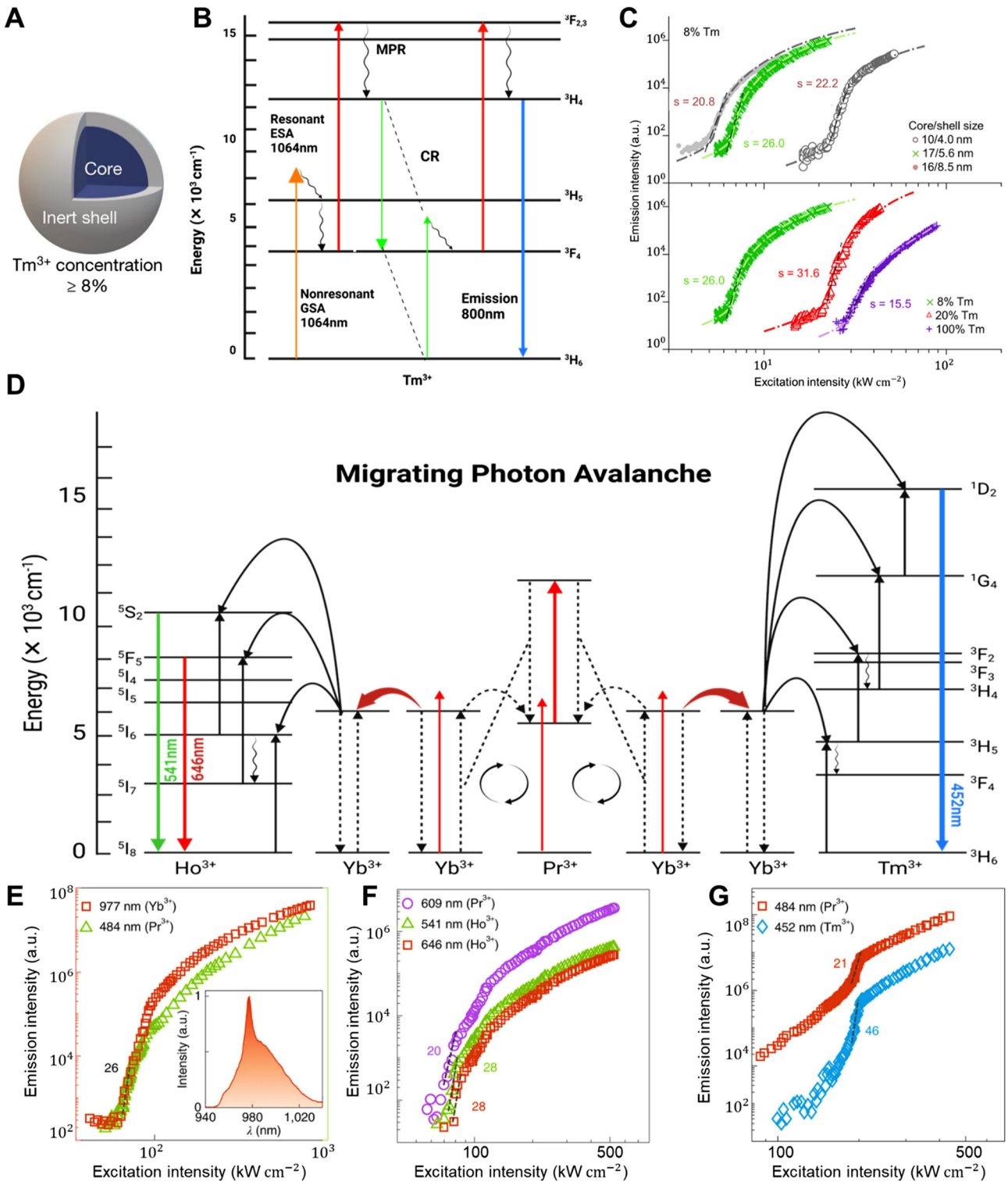

Fig. 5 PA in ANPs. (A) A schematic structure of 8% Tm^{3+}-doped core@shell ANP and (B) their proposed PA mechanism emitted the photons at 800 nm under 1064 nm photoexcitation. (C) A schematic plotting the graph of 800 nm emission intensity under λ_{ex} = 1064 nm for different core and shell sizes (top) for different Tm^{3+} ion concentrations (bottom), exhibiting 26th order optical nonlinearity with 8% Tm^{3+} ion-doped 17/5.6 nm core/shell size (green symbol). GSA, ESA, MPR, and CR denote the ground state absorption, the excited state absorption, multi-phonon relaxation, & cross-relaxation, respectively. Reproduced with permission from ref. 2. Copyright 2021, Springer Nature. (D) Schematic illustration of MPA mechanism where Yb^{3+}/Pr^{3+} ions migrate their avalanching energy to the Yb^{3+}/Tm^{3+} or Yb^{3+}/Ho^{3+} ions *via* the Yb^{3+} sublattice. (E–G) This cascade effect resulted in nonlinearity, which increased even more, up to the 46th order with a threshold of 120 kW cm^{-2} for the 452 nm emission for Tm^{3+} ion. Reproduced with permission from ref. 3. Copyright 2022, Springer Nature.

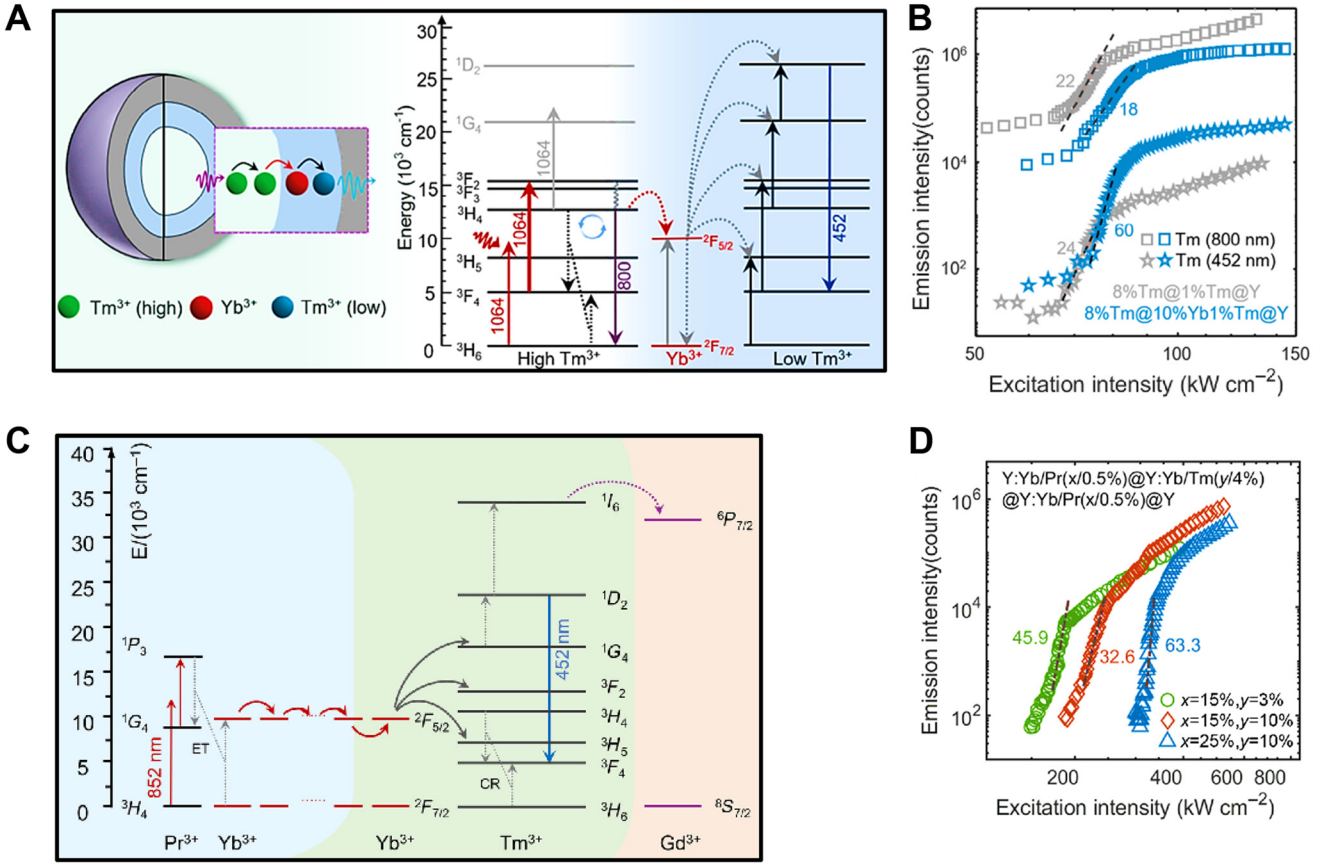

Fig. 6 PA in ANPs. (A) The nanostructure and the energy level diagram of the $Tm^{3+}/Yb^{3+}/Tm^{3+}$ system in which Yb^{3+} ions capture the avalanching energy from highly doped Tm^{3+} present in the core and relay that energy to the Tm^{3+} ions doped in the outermost shell that exhibits intense blue emission at 452 nm ($^1D_2 \rightarrow {}^3F_4$) under a 1064 nm photoexcitation, leading to 60th-order giant nonlinearity response (B) with an avalanching threshold of 45.6 kW cm^{-2}. Reproduced with permission from ref. 72. Copyright 2024, John Wiley and Sons (C) The energy transfer mechanism of the $Pr^{3+}/Yb^{3+}/Tm^{3+}/Gd^{3+}$ system upon the photoexcitation at 852 nm CW laser. (D) Emission intensity *versus* excitation intensity of Tm^{3+} ions at 452 nm exhibiting 63rd-order nonlinearity response. Reproduced with permission from ref. 73. Copyright 2024, SPIE Digital Library.

responses up to the 48th order, and the generation of full-spectrum avalanching emission across the visible range. This advancement deepened the understanding of the PA process and demonstrated the potential of enrePA for applications in diffraction-unlimited optical sensing, nanolasers, and optical data storage.

The progression of this research culminated in the development of a general cascade MPA mechanism, which achieved unprecedented optical nonlinearities through the strategic design of multi-layered nanostructures.[73] By incorporating a Gd^{3+} sublattice as a migrating network, the avalanching energy initiated within the core could propagate over long distances, inducing nonlinear optical responses in various emitters located within the shell layers. This approach enabled extreme optical nonlinearities up to the 63rd order from Tm^{3+} ions and the 45th order from other emitters such as Tb^{3+}, Eu^{3+}, Dy^{3+}, and Sm^{3+} Fig. 6(C and D). The resulting multi-color emissions facilitated super-resolution microscopic imaging with single-nanoparticle sensitivity and a lateral resolution of 48 nm using a single low-power 852 nm excitation beam.

Materials capable of responding to optical stimuli with high nonlinearity are essential for advancing technologies like super-resolution imaging and optical data storage. However, achieving extreme optical nonlinearity beyond a factor of 60 has been a significant challenge due to the complexity of the PA process, which is influenced by factors such as absorption cross-sections, CR dynamics, and electron–phonon interactions. To overcome this, Liu *et al.* significantly enhanced the optical nonlinearity of $NaYF_4$ nanocrystals doped with 15% Tm^{3+} ions by substituting Y^{3+} with Lu^{3+}, creating a $NaLuF_4$:Tm (15%) matrix.[74] This structural modification increased the material's optical nonlinearity from about 41 to 156, particularly for light emission 805 nm ($^3H_4 \rightarrow {}^3H_6$) Fig. 7(A and B). The enhancement was attributed to crystal field distortions caused by Lu^{3+}, which amplified ESA driven by electric dipole (ED) transitions while suppressing GSA dominated by magnetic dipole (MD) transitions. Additionally, the $^3F_{2,3}$ levels, which feed into the $^3H_4$ level, showed improved luminescence efficiency. This substantial boost in nonlinearity positions Lu^{3+}-doped PA nanocrystals as promising candidates for 3D

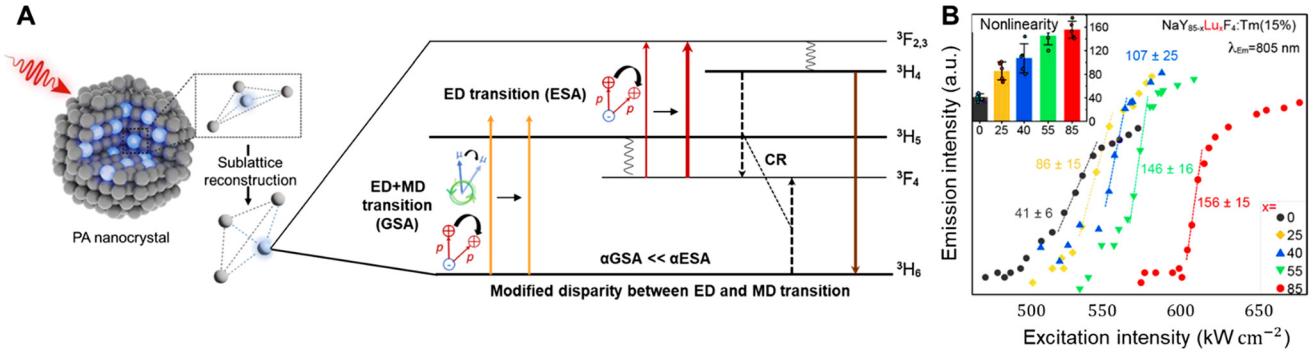

Fig. 7 PA in ANPs. (A) Schematic illustrating how lanthanide-induced lattice distortions in nanocrystals enhance the disparity between ED and MD transitions. This increases the rate of ED-favored optical transitions, boosting the ESA to GSA ratio, which is critical for optimizing photon avalanching efficiency, leading to extreme enhancement in nonlinearity response. (B) The inset displays the average optical nonlinearity based on five measurements. ED and MD represent the electric and magnetic dipoles. Reproduced with permission from ref. 74. Copyright 2024, Research Square (https://doi.org/10.21203/rs.3.rs-4183918/v1).

super-resolution imaging, drastically enhancing lateral and axial resolutions to 33 nm and 80 nm, respectively. These advancements set a new benchmark in imaging technology, enabling much finer detail and greater precision than ever before. The method is also cost-effective and requires simple equipment, making it a strong alternative to existing imaging techniques. Beyond imaging, these nanocrystals can be used in a variety of applications, including laser technology,[7] highly sensitive sensors,[159] and quantum optics,[156] offering exciting possibilities for the future.

There are still many unexplored aspects of ANPs, especially regarding their consistency in avalanching behavior and sensitivity to factors like environmental conditions, design parameters, and variations in nanocrystal structure. To address the issue of variability in ANPs, Kwock *et al.* focused on Tm^{3+}-based ANPs and studied how their design affects the differences in threshold intensity required for PA.[69] Using power-dependent imaging of single ANPs under CW laser excitation at 1064 nm, they developed a model to explain why these variations occur. The researchers observed that different ANP designs showed varying threshold intensities for PA. By analyzing single-particle imaging data and applying a surface energy transfer model, they found that differences in the thickness of the particle shell were the main cause of this variability. This study highlights how shell thickness influences the optical behavior of ANPs, suggesting ways to design nanoparticles with more consistent properties. These specially tailored ANPs, which utilize the PA process, could be more sensitive for environmental sensing applications than traditional UCNPs that rely on standard energy transfer mechanisms.

However, the optical characteristics of ANPs heavily rely on host matrices with low-phonon energies, which are crucial for minimizing multi-phonon relaxation (MPR) and tailoring the nonlinear response. Among the various host matrices available, fluoride matrices like β-$NaYF_4$ have been extensively used due to their relatively low phonon energy range (300–500 cm^{-1})[75] compared with alternative matrices like oxides (500–600 cm^{-1}),[76] oxysulfides (~520 cm^{-1}),[77] oxy-fluoride or -chloride (~500 cm^{-1}),[78] vanadates (~890 cm^{-1}),[79] and garnets (750–1000 cm^{-1}).[80] In comparison, halide-based host matrices, including chlorides, bromides, and iodides, exhibit even lower phonon energies (120–260 cm^{-1}). However, the synthesis of host matrices with significantly low phonon energies to minimize nonradiative relaxation and promote nonlinear response has serious challenges. Addressing this issue, Zhang *et al.* displayed a size-controlled synthesized Nd^{3+}-doped nanocrystal using a bromide host matrix (KPb_2Br_5:Nd^{3+}(16%)).[81] The resulting nanocrystal exhibited ultra-low phonon energies, reaching as low as 128 cm^{-1}. The remarkably low phonon energy of the nanocrystal played a crucial role in suppressing multiphoton relaxation, enhancing luminescence emission from higher excited states of Nd^{3+} ions, and facilitating highly nonlinear avalanche-like emission in the visible and NIR wavelength region at 595 nm ($^4G_{7/2}$/$^4G_{9/2}$ → $^4I_{11/2}$), 810 nm ($^4F_{5/2}$ → $^4I_{9/2}$) and 910 nm ($^4F_{3/2}$ → $^4I_{9/2}$) along with PA nonlinearity reaching >11, showing steeply nonlinear PA emission at 810 nm above a threshold of 10 kW cm^{-2}. These perovskite-like nanocrystals are stable under high humidity.

Another piece of research has been reported by Chen *et al.* that improved PA luminescence and optical nonlinearity in perovskite-type fluoride matrix $KMgF_3$ through the introduction of lanthanide ions *via* aliovalent doping.[82] Using KHF_2 pyrolysis, they synthesized core/shell $KMgF_3$ nanoparticles with tunable sizes and minimal OH^- defects. The utilization of KHF_2 precursor not only facilitated the spontaneous formation of $KMgF_3$:Ln^{3+} core/shell nanoparticles but also effectively removed internal OH^- defects from nanoparticles, which resulted in highly efficient red and green luminescence with quantum yields of ~3.8% and ~1.1%, respectively, under 980 nm excitation (0.02 kW cm^{-2}). KHF_2 also increased the energy transfer rate between Ln^{3+} ions, boosting PA luminescence at 802 nm under 1064 nm excitation. The resulting nanoparticles achieved a substantial nonlinearity up to the 27th order, with a threshold of 16.6 kW cm^{-2}.

Skripka *et al.* developed low-phonon-energy KPb_2Cl_5 nanoparticles doped with Nd^{3+} ions (16%) that showed purely

optical, nonlinear, and bistable luminescence without thermal contributions.[83] These nanoparticles exhibited intrinsic optical bistability (IOB), which enabled them to switch between two stable luminescent states: a dark, non-emissive state and a bright, upconverted emissive state, under a single 1064 nm photoexcitation Fig. 8(A and B). The bistability arose from positive PA feedback which stabilized the bright state with a sharp emission at 810 nm with a threshold value of 6.7 kW cm^{-2}, resulting in over 200th-order optical nonlinearity at 77 K. This behavior is attributed to the suppression of non-radiative relaxation in Nd^{3+} ions and the PA feedback process Fig. 8(C and D). Conversely, the dark state is stabilized by non-radiative quenching. By modulating hysteresis behavior through adjustments in excitation parameters, such as low-duty cycles and scan rates, the nanoparticles achieved efficient luminescence switching and high-contrast optical functionality. This enables their operation as nanoscale optical transistors and holds significant potential for applications in digital optical computing,[84] neuromorphic circuits,[85] imaging, and photonic technologies.[4,86] Their low-phonon-energy composition further enhances their stability and performance, enabling integration with telecommunication systems and advanced photonic platforms,[87,88] offering a promising foundation for next-generation optical logic and computing solutions.

The ability to achieve the PA effect at the nanoscale has great potential for various applications, such as sub-diffraction imaging,[4] nano thermometry,[5] and the development of nano- and micro-laser.[7] To fully harness the benefits of PA effects and customize them for specific needs, it is crucial to conduct comprehensive research to understand the chemical and physical factors influencing PA behavior. A recent study by Dudek *et al.* focused on investigating these factors at three different length scales: avalanching nano, micro, and bulk crystals doped with 3% or 8% of Tm^{3+} ions[68] Fig. 9(A). The researchers used experimental and theoretical modeling

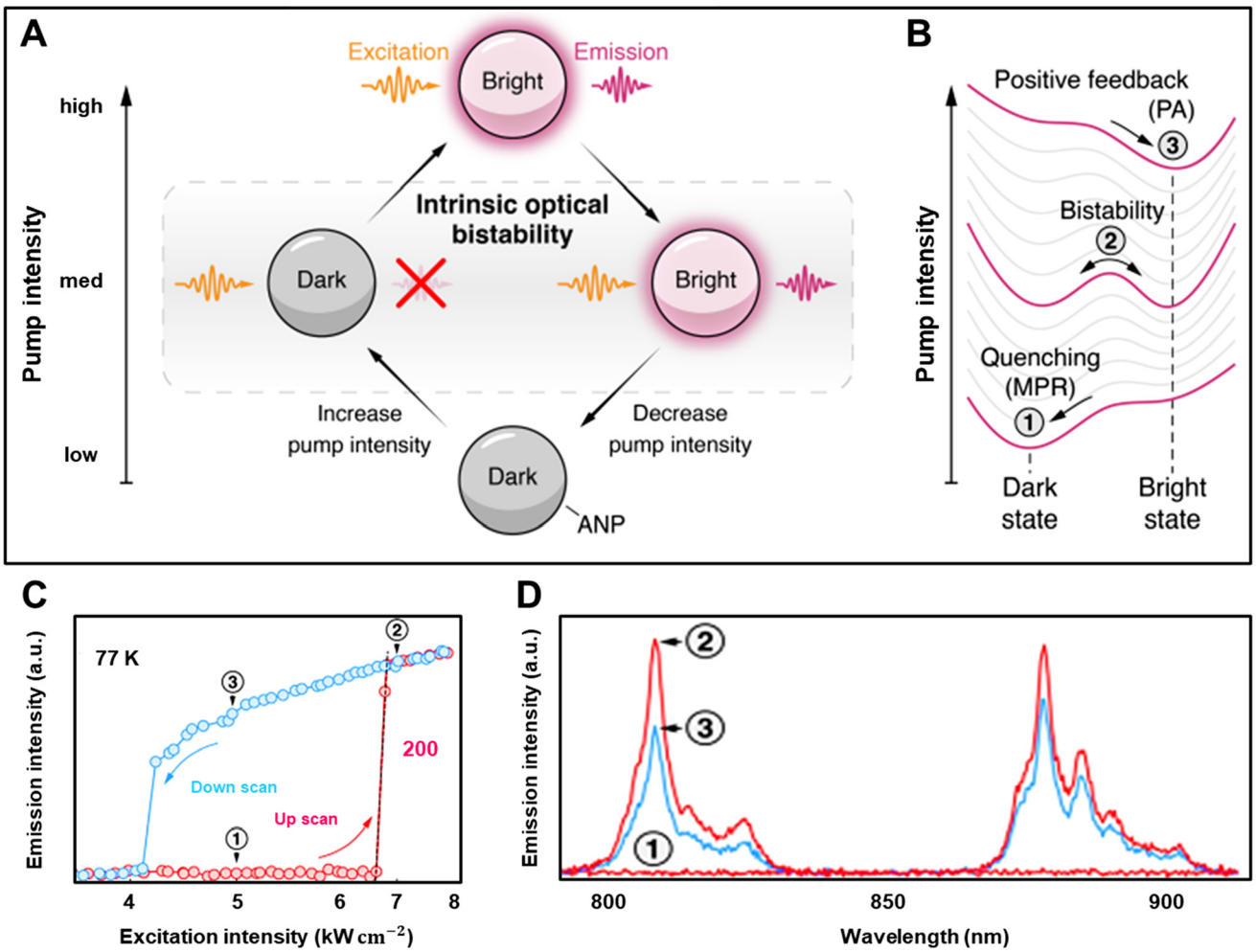

Fig. 8 PA in ANPs. (A) A schematic illustration of bistable luminescence in ANPs, showing a switch from a dark state to a bright state under 1064 nm excitation. (B) The energy landscape of ANPs at various pump intensities: the dark state (1) is stabilized by non-radiative quenching, while the bright state (3) is maintained by a positive feedback loop, leading to PA with an extreme nonlinear response exceeding 200th-order at 77 K (C) and sharp luminescence peak at 810 nm corresponding to the ($^4F_{5/2} \rightarrow {}^4I_{9/2}$) transition (D). Reproduced with permission from ref. 83. Copyright 2024, arXiv (https://doi.org/10.48550/arXiv.2403.04098).

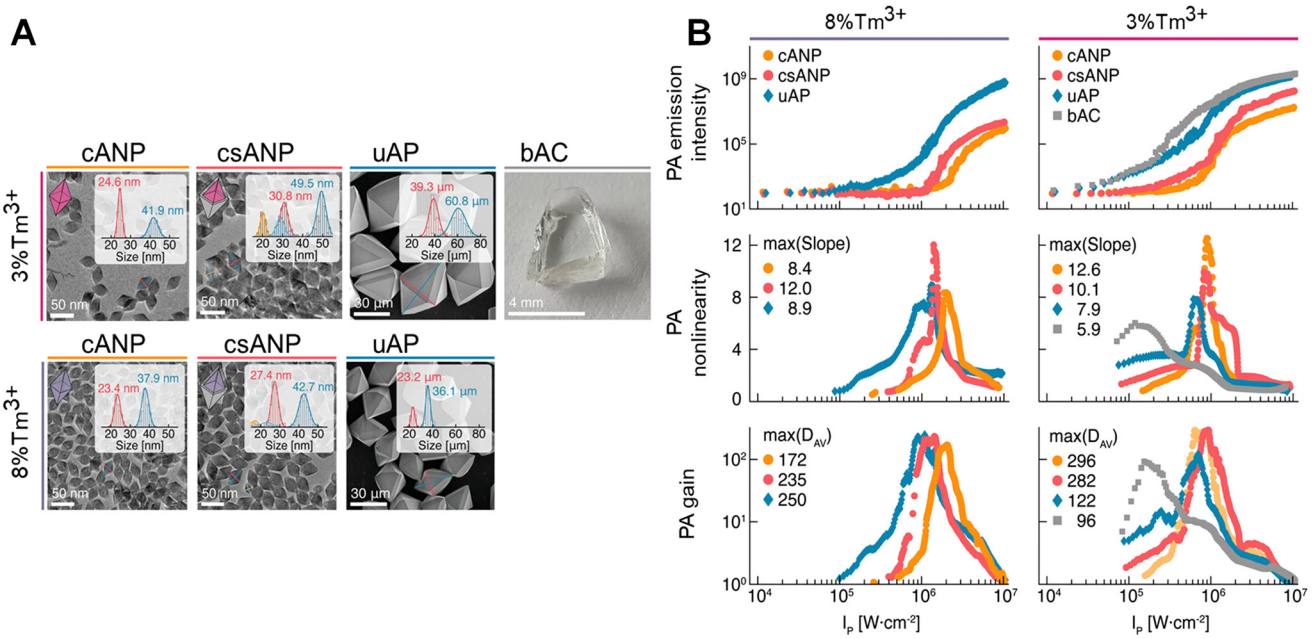

Fig. 9 Size-dependent PA. (A) Cartoon images showing the morphology of cANP, csANP, uAP, and bAC doped with 3% of Tm^{3+} ion (top) and 8% of Tm^{3+} (Bottom). Based on the average dimensions of the nanocrystals, the thickness of the shell is 3.1 and 2 nm in width and 3.8 and 2.4 nm in length, for 3% Tm^{3+} and 8% Tm^{3+}-doped csANPs, respectively. (B) Comparison of pump power-dependent PA emission intensity (graph 1), PA slopes (graph 2), and PA gains (graph 3) at 800 nm for the 8% and 3% Tm^{3+}-doped materials cANP, csANP, μAP, and bAC. Reproduced with permission from ref. 68. Copyright 2022, John Wiley and Sons.

approaches to analyze the PA effect. They observed highly nonlinear PA emission of Tm^{3+} ion at 475 nm and 800 nm when excited with a 1064 nm wavelength in all avalanching materials. Interestingly, the order of optical nonlinearity was found to be greater than 12 in avalanching core–shell nanoparticles, compared with avalanching micro (S = 8.9) and bulk crystals (S = 5.9) Fig. 9(B). This suggests that the nano-sized core–shell nanoparticles exhibited the highest order of optical nonlinearity among the three materials. Furthermore, the properties of the PA process, such as optical nonlinearity, PA gain, PA intensity, and luminescence kinetics, showed a dependence on the crystal volume and surface quenching.

3. Emerging sub-diffraction imaging applications of ANPs

ANPs have received a lot of attention lately because of their distinctive characteristics, such as remarkable nonlinear efficiency, the ability to emit light with an anti-Stokes shift, to reduce signal-to-noise ratios, and background noise in imaging and sensing applications. Additionally, ANPs exhibit resistance to photobleaching and photoblinking, ensuring their longevity and reliability compared with other fluorescent probes. Moreover, their unique ability to penetrate deep into tissues and their photostability and biocompatibility have opened new avenues for applications in deep-tissue imaging. A standout feature of ANPs is their intrinsic forbidden transitions within the 4f states, resulting in prolonged lifetimes of excited energy levels. This characteristic allows for tunable lifetimes, facilitating optical imaging with exceptional spatiotemporal resolution, making it an ideal tool for temporal domain imaging. In this section, we delve into the fascinating world of optical imaging techniques utilizing avalanche nanomaterials, transcending the boundaries of super-resolution imaging, including STED, STORM, SIM, SMLM, PALM, MINFLUX, and extending to the realms of deep tissue imaging and lifetime imaging, as well as single-particle imaging and tracking. Through this exploration, we aim to shed light on the remarkable capabilities and immense potential of ANPs in revolutionizing the field of optical imaging.

3.1. Single-particle super-resolution imaging

Super-resolution imaging is a revolutionary technique that surpasses the limits of diffraction of traditional microscope techniques and enables the investigation of biological structures and processes in unprecedented detail.[89–91] Conventional microscopy such as confocal laser microscopy has been widely utilized in fluorescence microscopy due to its non-contact, non-invasive nature, and high specificity, making it an excellent tool for visualizing specific biological molecules and their interactions in life science research. However, its resolution has historically been limited by the diffraction of light, which imposes a resolution limit of approximately half the wavelength of the light employed in imaging.[92,93] However, recent breakthroughs in super-resolution modalities that operate beyond this diffraction limit, such as Stimulated emission depletion (STED) microscopy,[94–96] Photoactivated localization

Table 3 Comparison of ANPs with other fluorescent probes based on key performance metrics, advantages, limitations, and typical applications

Material	Excitation threshold	Signal-to-noise ratio	Photostability	Emission efficiency	Background interference	Applications	Cost and synthesis	Ref.
Fluorescent proteins	Low	Moderate	Poor	Moderate	High	Live-cell imaging	Low-cost, easy	102
Traditional UCNPs	Moderate	Moderate	Good	High	Moderate	Bioimaging, lasers	Moderate, complex	103
Organic dyes	Low	Low	Poor	Moderate	High	Bioimaging FRET	Low-cost, simple	104 and 105
QDs	Moderate	Moderate	Moderate	High	Moderate	Bioimaging, displays	Expensive, simple	106
ANPs	High	Very high	Excellent	High	Low	Super-resolution imaging, deep-tissue imaging	Expensive, complex	107

microscopy (PALM),[97,98] Stochastic optical reconstruction microscopy (STORM),[99] Structured illumination (SIM),[100] and Single-molecule localization microscopy (SMLM)[101] have shattered these limitations, allowing us to delve into the realm of nanoscale imaging. Conventionally, super-resolution modalities heavily rely on fluorescent proteins, QDs, several organic molecular dyes, and conventional UCNPs.[102–106] These reporters have several limitations regarding brightness, toxicity, and photostability within the cellular environment (Table 3). However, a recent and exciting development lies in the use of lanthanide-doped ANPs as a promising alternative for super-resolution imaging because they exhibit intense light in deep-UV-to-Vis and NIR regions at relatively low excitation NIR light, owing to the induced positive optical feedback system in each nanocrystal. This enables the experimental realization of photon-avalanche super-resolution imaging with sub-nanometer spatial resolution, surpassing the diffraction barrier originally described by Ernst Abbe. Also, ANPs possess excellent photostability, resist photobleaching, and experience minimal scattering.[107]

A pioneering study by Liu *et al.* introduced the concept of the pre-avalanching phenomenon using 8% Tm^{3+}-doped UCNPs for sub-diffraction imaging, offering a groundbreaking approach for super-resolution nanoscopy.[108] Their innovative dual-laser confocal system employed a 980 nm excitation beam which established the population inversion between the intermediate ($^3H_4$) state and ground ($^3H_6$) state of Tm^{3+} ions, triggering a PA-like effect. By illuminating the nanoparticles with a depletion beam at 808 nm, matching the upconversion band of the $^3H_4 \rightarrow {}^3H_6$ transition, they induced amplified stimulated emission and achieved remarkable single-nanoparticle detection at 28 nm resolution, which is the $1/36^{th}$ power of the wavelength. This simplified optical layout surpassed previous methods based on traditional upconverting nanomaterials. In contrast, another interesting investigation has been reported by Zhan *et al.*, who introduced highly efficient optical emission depletion nanoscopy by assisting CR in $NaYF_4$ nanoparticles doped with a substantial 10% concentration of Tm^{3+} which substantially reduced the laser intensity needed for optical depletion emission.[109] Leveraging this novel emission depletion technique, they achieved two-color super-resolution imaging with a remarkable resolution of 66 nm using only a single pair of excitation and depletion beams, and successfully imaged immunostained cytoskeleton structures in fixed cells, achieving a lateral resolution of approximately 82 nm. On the other hand, Li *et al.* investigated silica-coated Ga(III)-doped ZnO: Yb^{3+},Tm^{3+} nanoparticles for high-resolution *in vivo* imaging of myocardial tissue in the NIR region.[110] As an activator, Tm^{3+} ions emitted 830 nm in the NIR region under a 980 nm laser source. Intravenous injection of 6 mg kg^{-1} silica-coated Tm^{3+} nanoparticles in myocardial tissue produced a red NIR fluorescence image with strong brightness and showed no observable lesions, abnormalities, or signs of toxicity even after 7 days. The silica shell-coated nanoparticles effectively mitigated concentration quenching and amplified the NIR emission intensity of particles, exhibiting a highly nonlinear response to increasing density powers. This phenomenon indicated the occurrence of PA of Tm^{3+}, resulting in a remarkable over 12-fold enhancement in NIR luminescence intensity compared with conventional UCNPs. These findings underscored the promising potential of Yb/Tm/GZO@SiO_2 nanoparticles for bioimaging applications, with the silica shell coating notably enhancing the biocompatibility of the nanoparticles.

However, Lee *et al.* successfully demonstrated single-particle imaging of ANPs,[2] using the recently proposed PASSI concept by Bednarkiewicz *et al.*[26] This method takes advantage of the extreme nonlinear response of PA to achieve a spatial resolution of less than 70 nm using standard scanning confocal microscopy (SCM), without requiring any computational processing. In SCM, the resolution depends on the order of nonlinearity S of the emitter, following an inverse square root relationship similar to multiphoton microscopy. The resolution, expressed as the full-width at half-maximum (FWHM) of the imaging point, can be estimated using the formula:

$$\mathrm{FWHM} = \lambda/(2\mathrm{NA}\sqrt{S}) \quad (1)$$

where λ is the light's wavelength, and NA is the numerical aperture of the objective lens. This means ANPs can provide extremely high resolution automatically during standard SCM, without needing specialized equipment, beam shaping, image corrections, or alignment procedures. Thus, in this study, imaging of single ANPs achieved a resolution (spot size) of

75 nm or less when excited at a wavelength of 1064 nanometers with optimal intensity Fig. 10(A and B). For ANPs doped with 8% Tm^{3+} ions and a nonlinearity S = 26, the FWHM of the short axis of the spot was 65 ± 7 nm, and the long axis was 81 ± 9 nm. The slightly elliptical shape of the spot was due to the shape of the excitation beam Fig. 10(B). These results matched well with theoretical predictions and simulations Fig. 10(D–F). When the excitation intensity was closer to the saturation regime, where S was lower, the spot size increased to about 220 nm, as shown in Fig. 10(A and D). The theoretical limit for a system with S = 26 is calculated to be 70 nm, which agrees closely with the experimental results. These findings highlight the potential of ANPs for applications in super-resolution imaging and local environmental, optical, and chemical sensing.

Moreover, Liang *et al.* and Wu *et al.* have contributed significantly to the development of Migrating Photon-Avalanche super-resolution nanoscopy, a powerful low-power imaging technique that utilizes a single NIR CW laser for super-resolution imaging of single nanoparticles.[3,73] Liang *et al.* demonstrated the use of a standard multiphoton microscope integrated with an 852 nm CW laser beam Fig. 11(A) to achieve a lateral resolution of 62 nm, (approximately $\lambda/14$), at a low excitation intensity of 76 kW cm^{-2}, while maintaining excellent photostability[3] Fig. 11(B–J). A notable advantage of this method is the rapid response time of MPA nanoparticles, enabling fast laser scanning and practical imaging over large fields of view. The researchers also successfully imaged subcellular actin filaments in HeLa cells by labeling them with MPA nanoparticles conjugated with phalloidin molecules. This approach revealed intricate details of the actin fibers with a resolution of 71 nm Fig. 11(K–O). The low-power 852 nm excitation beam, falling within the biological transparency range, minimized heating effects, making the technique highly suitable for *in vitro* bioimaging applications.

Building on this, Wu *et al.* reported multi-color cascade Migrating Photon-Avalanche super-resolution microscopy, which achieved imaging of single MPA core/shell nanoparticles doped with various emitter ions[73] (Pr^{3+}, Tm^{3+}, Tb^{3+}, Eu^{3+}, Dy^{3+}). This technique demonstrated sub-nanometer resolution under a single 852 nm CW excitation beam, showcasing exceptional sensitivity and resistance to photobleaching. At the 452 nm emission of Tm^{3+} ions, a lateral resolution of 48 nm ($\lambda/17$) was achieved at an excitation intensity of 320 kW cm^{-2} Fig. 11(P(a)). In comparison, a diffraction-limited resolution of 225 nm was observed at a high-power laser intensity of 1403 kW cm^{-2}, signifying a five-fold improvement in Fig. 11 (P(b)). Similarly, imaging at 605 nm emission from Pr^{3+} ions showed a three-fold improvement in lateral resolution of 81 and 230 nm Fig. 11(R(a and b)), further confirming that the higher nonlinearity order of PA in Tm^{3+} ions contributed to the superior resolution. Together, these studies underscore the

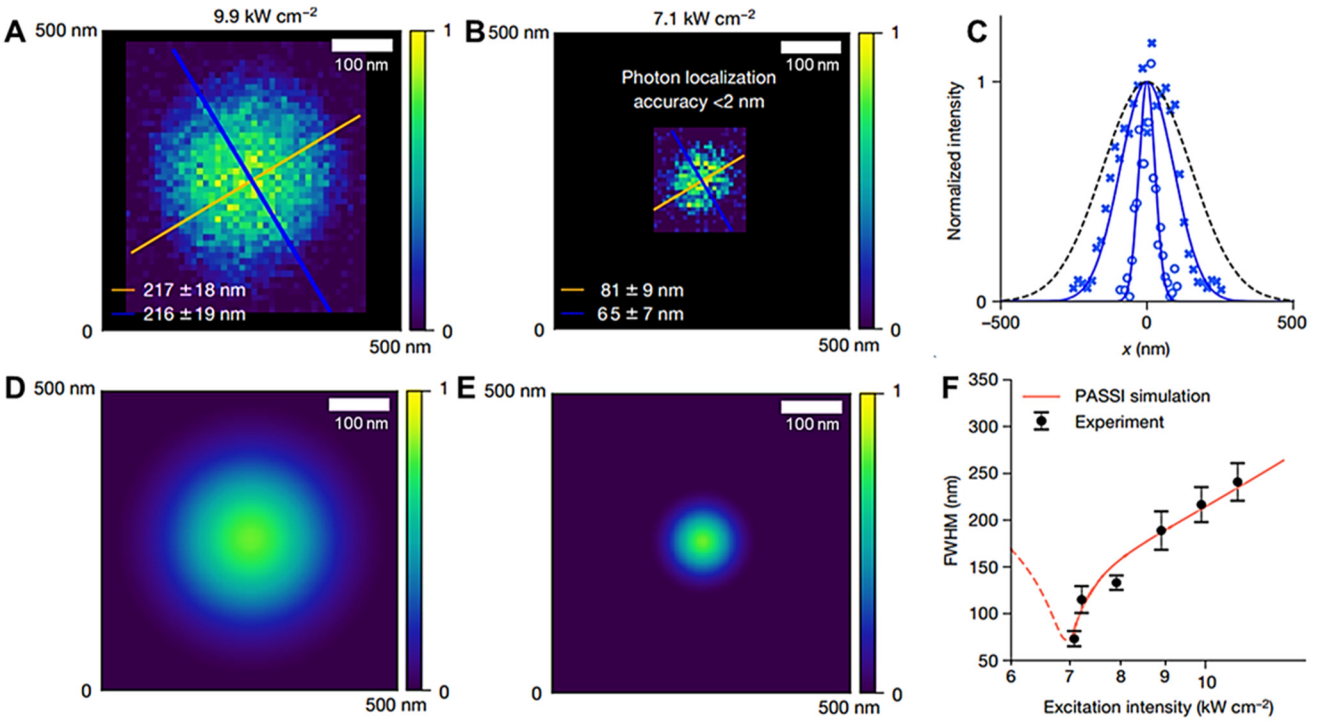

Fig. 10 Photon-avalanche single-beam super-resolution imaging. (A) Single-ANP images excited under 1064 nm pump intensity at 9.9 kW cm^{-2} (B) at 7.1 kW cm^{-2}. (C) Line cuts corresponding to the blue lines in panels (A) and (B), along with a line cut through a theoretically diffraction-limited Gaussian focal spot. (D and E) ANP images are based on theoretical modeling under the same excitation wavelength and power intensities. (F) Comparison of measured (black) and simulated (red) FWHMs of single-ANP PASSI images across different excitation intensities. Reproduced with permission from ref. 2. Copyright 2021, Springer Nature.

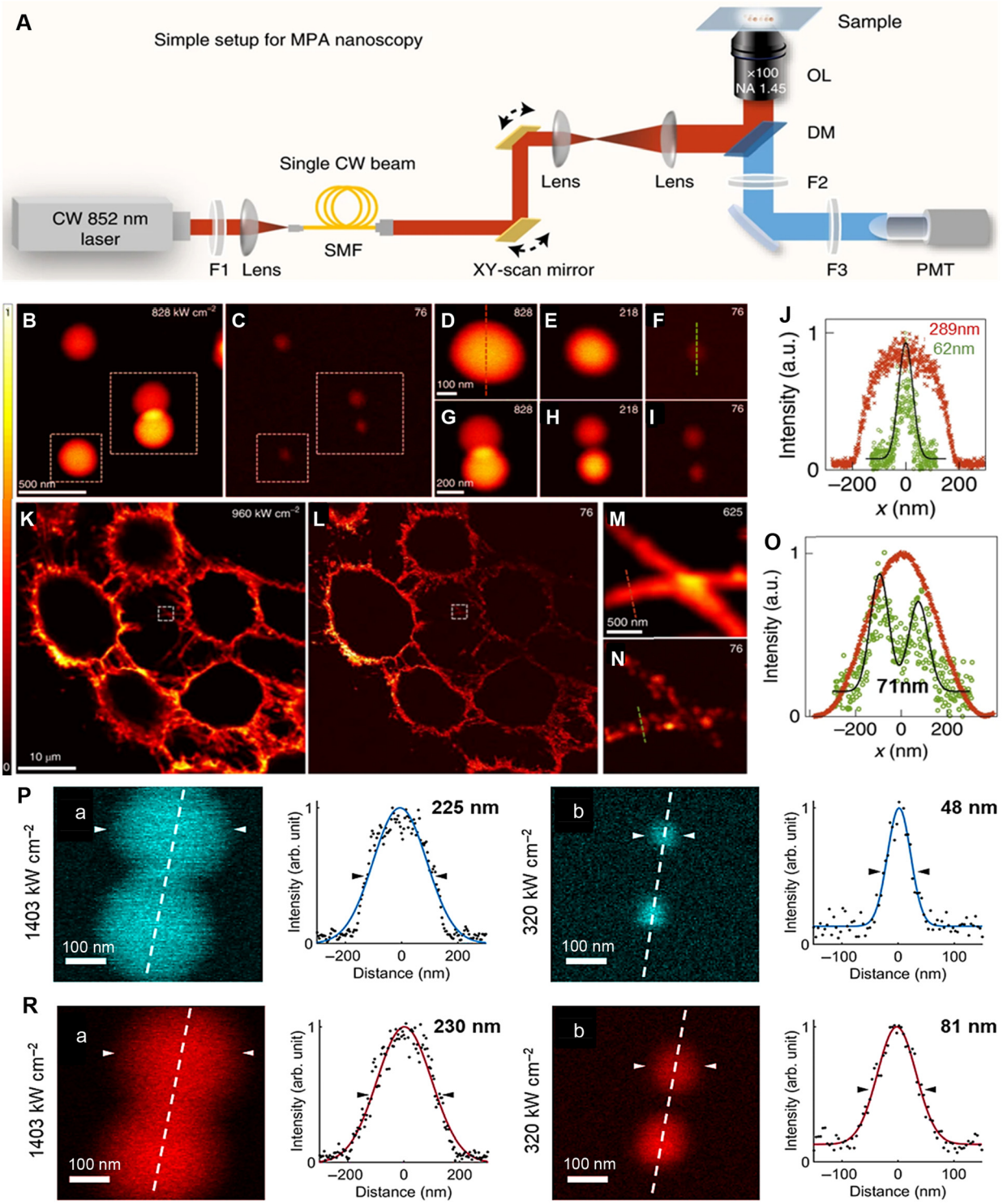

Fig. 11 Migrating photon avalanche super-resolution nanoscopy. (A) Schematic illustration of confocal laser scanning microscope coupled with single CW 852 nm laser beam. OL represents 100× NA = 1.45 oil-immersed objective lens; PMT represents Photomultiplier tube, DM represents 690 nm short-pass dichroic mirror; F1 represents 850/10 nm band-pass filter; F2 represents 694 nm short-pass filter; F3 represents 665 nm short-pass filter; SMF represents Single-mode fiber. (B and C) Single-particle imaging of 26 nm MPA at 828 kW cm^{-2} over the threshold (B), and at 76 kW cm^{-2} close to the PA region (C). (D–I) Magnified images of individual nanoparticles marked by white-colored box, at excitation powers (828, 218, and 76 kW cm^{-2}). (J) Line profile analyses of areas marked by dashed lines in (D) and (F), revealed 62 nm lateral resolution at 76 kW cm^{-2} excitation power. (K–L) Imaging of actin filaments of HeLa cells immunolabelled with phalloidin-conjugated nanoprobes. (M–N) Magnified images of the white-colored box in (K) and (L). (O) Line profile analyses of the dashed line in (M) and (N). Reproduced with permission from ref. 3. Copyright 2022, Springer Nature. (P) Single-particle imaging of Tm^{3+}-doped MPA at 1403 kW cm^{-2} (a) and 320 kW cm^{-2} (b), revealing 48 nm resolution. (R) Single-particle imaging of Pr^{3+}-doped MPA at 1403 kW cm^{-2} (a) and 320 kW cm^{-2} (b), revealing 81 nm resolution. MPA represents Migrating Photon Avalanche. Reproduced with permission from ref. 73. Copyright 2024, SPIE Digital Library.

potential of MPA super-resolution microscopy for high-resolution, low-power imaging, offering unparalleled advantages such as enhanced photostability, multi-color imaging capability, and minimal heating effects for practical applications.

In a subsequent study, Lee *et al.* presented a groundbreaking advancement in super-resolution imaging.[4] They successfully employed indefinite NIR Photon-Avalanche localization microscopy (INPALM) to achieve sub-Å localization super-resolution imaging of photoswitched Tm^{3+}-doped ANPs as well as their cluster where three ANPs are tightly packed. Unlike single-molecule localization microscopy (SMLM), the accuracy of IN-PALM is not constrained by the limited number of photons collected before photobleaching. This is due to the active control of the emitting ANP concentration, which is maintained at a very low level. By ensuring that only a subset of probes emits photons at any given time, non-overlapping point spread functions are achieved, enabling precise centroid fitting, and significantly enhancing localization accuracy. A distinguishing feature of IN-PALM is the reversible photoswitching of ANPs. Unlike SMLM methods that suffer from irreversible photobleaching, ANPs can be repeatedly brightened and darkened at 1064 nm and 400–840 nm, respectively. This capability greatly expands the number of collected photons (1.33×10^8 approx) without signs of degradation, leading to substantial improvements in localization accuracy. Leveraging the power of IN-PALM, the researchers achieved impressive results. The researchers observed a single ANP image with localization accuracy <1 Å, surpassing the diffraction limit. Furthermore, they successfully obtained diffraction-limited images at sub-Å localization super-resolution of ANP clusters through iterative photoswitching cycles that allowed them to discern three separate nanoparticles inside densely packed clusters Fig. 12(A and B).

Researchers have made significant progress in surpassing the diffraction limit of light in two dimensions (2D) using techniques like standard confocal laser microscopy,[2,26] multi-photon microscopy,[3] or PA-based microscopy[4,26] coupled with single or dual beams, achieving resolutions as small as sub-nanometer. However, breaking the diffraction limit in three dimensions (3D) remains a challenge. Improving 3D imaging resolution requires enhancing both axial (depth) and lateral (side-to-side) resolution beyond the limits defined by the FWHM of the PSF. To address this, Liu *et al.* introduced a method called mirror-assisted self-interference field excitation (SIEx), a highly nonlinear super-resolution microscopy technique.[111] This approach allows for isotropic 3D imaging using just a single objective lens and one laser beam. The technique uses a mirror to create self-interference during excitation, generating a spherical focal spot for precise imaging Fig. 13(A). In experiments, researchers used giant nonlinear respond (S = 33) ANPs as fluorophores and an 852 nm CW, NIR laser beam (19 kW cm^{-2}). This setup achieved a remarkable 3D imaging resolution of 54 nm laterally and 57 nm axially (both around λ/15) Fig. 13(B–E). The team extended the applicability of this technique to biological imaging, achieving super-resolution imaging of immunolabeled actin filaments (50–150 nm) of

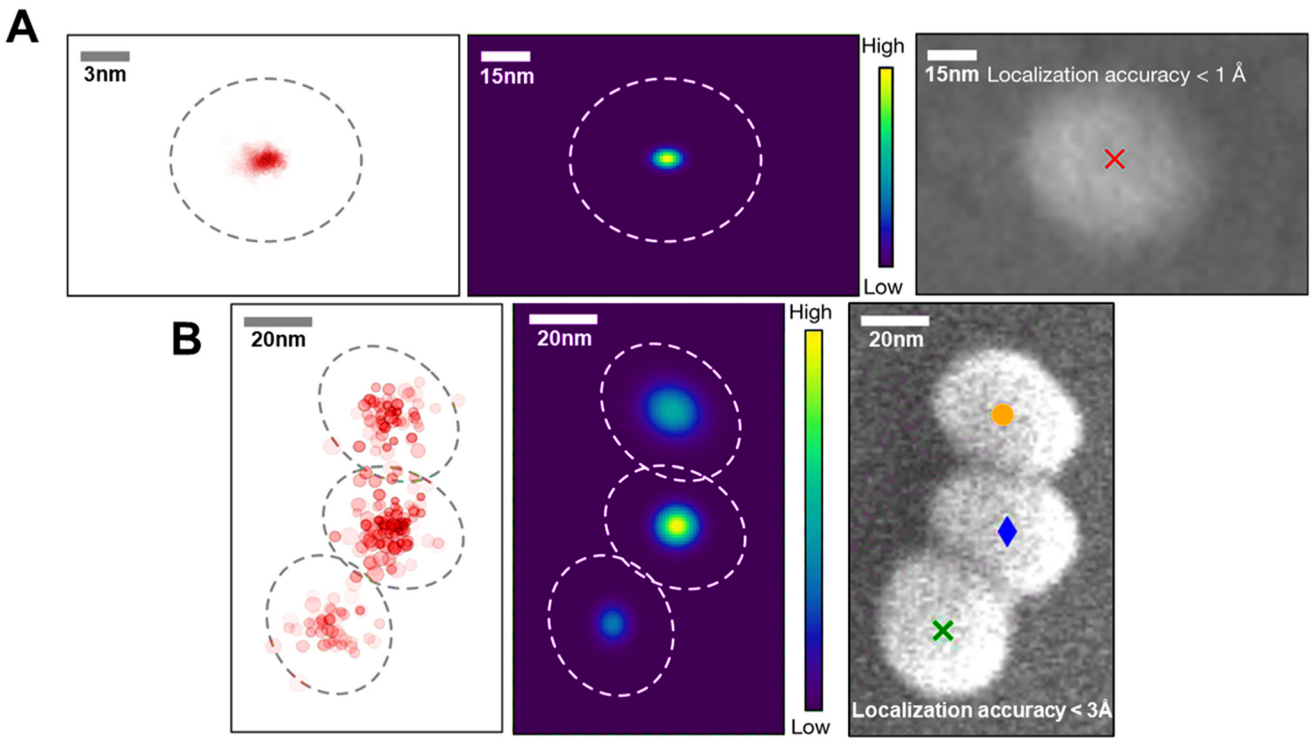

Fig. 12 Indefinite NIR photon-avalanche localization microscopy. (A) Imaging of single-ANPs and (B) imaging of its cluster using the IN-PALM method. Reproduced with permission from ref. 4. Copyright 2023, Springer Nature.

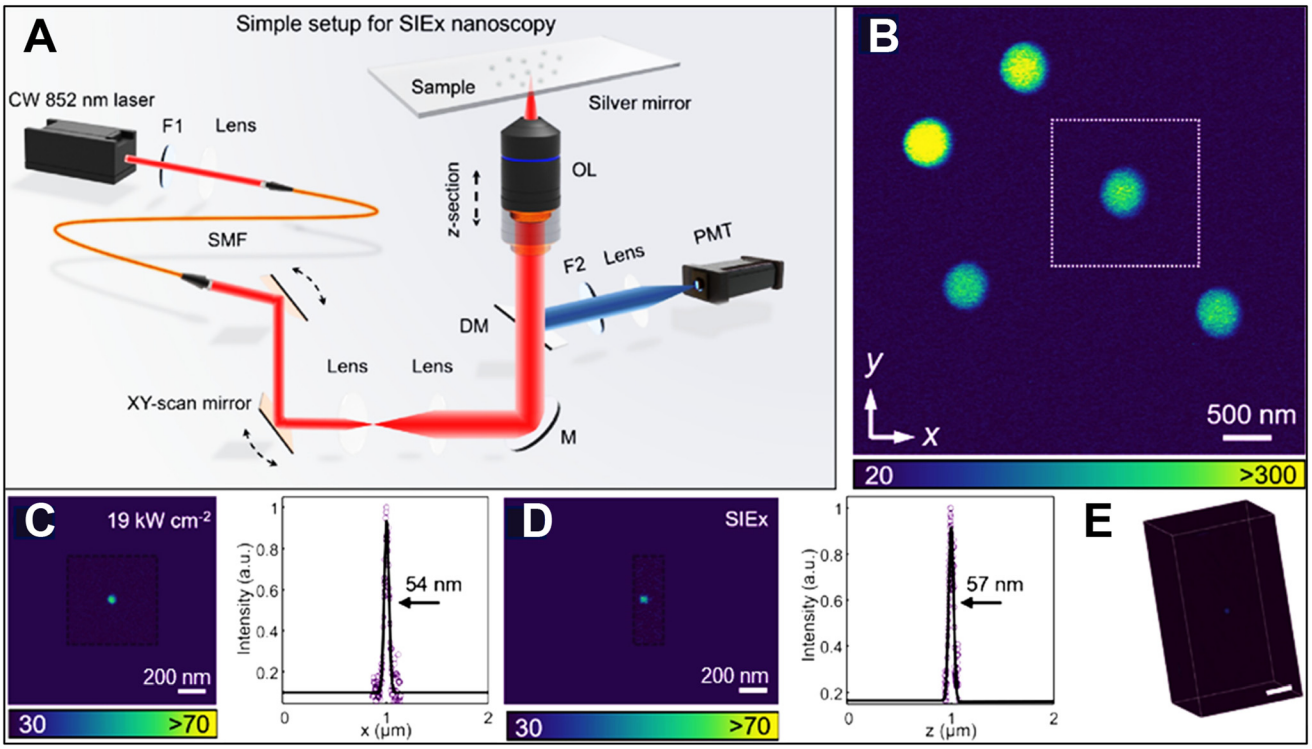

Fig. 13 Self-interference field excitation (SIEx) super-resolution nanoscopy. (A) Schematic illustration of conventional confocal laser scanning microscope coupled with low-power, single CW 852 nm laser beam. OL represents 100× NA = 1.45 oil-immersion objective lens; PMT represents Photomultiplier tube, DM represents 690 nm short-pass dichroic mirror; F1 represents 850/10 nm band-pass filter; F2 represents 665 nm short-pass filter; F3 represents 665 nm short-pass filter; SMF represents single-mode fiber. (B) Imaging of single ANP distributed on a silver mirror in (A) under an 852 nm excitation beam above the PA threshold. (C and D) Magnified images and resolution of single ANP marked by white square box in (B) employing SIEx technique under an excitation intensity power of 19 kW cm^{-2} exhibiting resolution of 54 nm laterally (C) and 57 nm axially (D). (E) Corresponding 3D *z*-stack showing the PSF of a single ANP in 3D space. Reproduced with permission from ref. 111. Copyright 2024, Optica Publishing Group.

BSC-1 cells. Using phalloidin-conjugated ANPs, they obtained a lateral resolution of 67 nm and an axial resolution of 71 nm, (both less than $\lambda/13$) Fig. 14(A–I). Integrating the SIEx method with modern 3D biological imaging techniques could enable higher-resolution imaging while using lower power and simpler equipment, making it a valuable tool for advancing life science research and light microscopy applications. In the future, combining SIEx with advanced cellular labeling and bioconjugation methods[112–114] could further enhance its applications. The photostability, minimal autofluorescence, and high optical nonlinearity of ANPs make them an invaluable tool for studying membranes and other biological structures.

3.2. Deep-tissue imaging

Deep-tissue imaging involves employing optical imaging methods to observe the inner workings and structures of living tissue, including organs and tumors, situated at significant depths.[115] This is accomplished by utilizing imaging modalities capable of penetrating biological tissue. In recent times, optical imaging utilizing NIR light has emerged as a highly promising technique for visualizing biological processes within deep tissue. The low energy levels of NIR radiation and its limited tendency to induce autofluorescence make it an ideal choice for such imaging applications.[116] In contrast to visible light, the low scattering and absorption of NIR photons by typical tissues enable imaging of micron-scale features through millimeters of a sample. Most of the recent exploration of NIR imaging has focused on the NIR-II window: the 1000–1400 nm region of the spectrum that exhibits high transmission in tissue. In this regard, lanthanide-doped nanomaterials hold promise as effective probes for deep imaging due to their stable emission in the visible and NIR regions.[117–119] However, these materials face limitations in efficiently absorbing NIR-II wavelengths because of the lack of lanthanide GSA transition in this range. So, to overcome this problem, Levy *et al.* introduced a new class of materials, so-called energy-looping nanoparticles (ELNPs), that induced the PA effect under non-resonant 1064 nm photoexcitation with ESA, rather than GSA.[37] This looping process occurred in $NaYF_4$ energy-looping particles doped with 20% of Yb^{3+} (sensitizer) and 0.5% of Tm^{3+} (activator) that emitted emission at 800 nm Fig. 15(A). By employing this gentle excitation approach in conjunction with standard confocal microscopy, the researchers successfully imaged ELNPs within live mammalian cells and mouse brain tissue without interference from autofluorescence. Impressively, the imaging depths reached

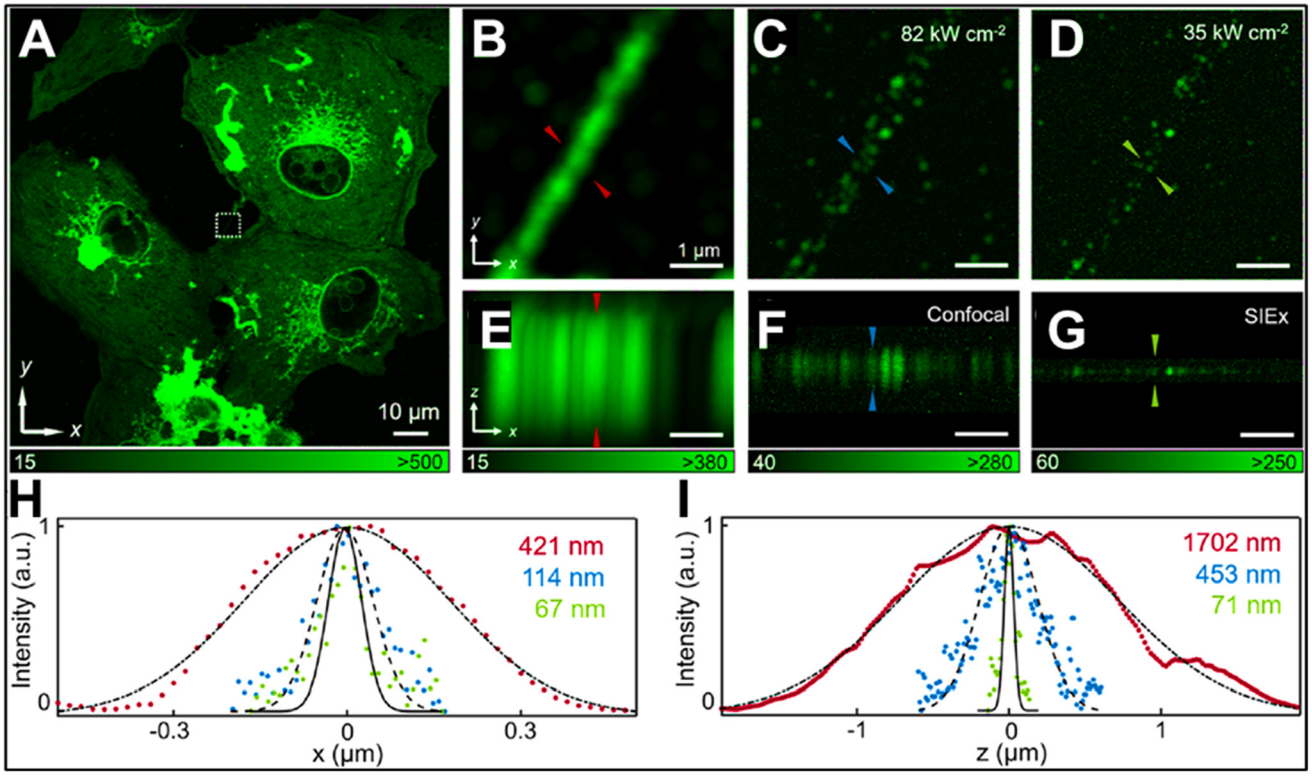

Fig. 14 3D super-resolution imaging of immunolabelled actin filaments of BSC-1 cells with phalloidin-conjugated ANPs on a silver mirror by employing a SIEx setup. (A) Imaging of filaments under an 852 nm CW NIR excitation beam. (B–D) Magnified views of filaments marked by white square box in (A) under different excitation power intensities of 1169 kW cm^{-2}, 82 kW cm^{-2}, and 35 kW cm^{-2}. (E–G) Axial views of corresponding views in (B–D) under the same excitation power intensities. (H and I) Corresponding lateral and axial Line intensity profiles of the features in (B–G). Reproduced with permission from ref. 111. Copyright 2024, Optica Publishing Group.

1 mm, while the achieved feature sizes of 2 μm were comparable to those achieved using state-of-the-art multiphoton techniques Fig. 15(B–D). These results highlight the potential of ELNPs as a promising class of NIR probes for precise visualization in cells and tissues. Introducing an energy migration lattice in a nanoparticle can tune the lifetime of upconversion emissions. The $NaYF_4$@$NaYbF_4$@$NaYF_4$:Yb/Tm@$NaYF_4$ nanoparticles exhibit tunable lifetimes by modifying the thicknesses of the energy migration layer and Yb^{3+} concentration in the energy transfer upconversion region for *in vivo* upconversion imaging. This method also offers a solution for the lifetime tuning of down-shifting emissions, as evidenced in the ability of core–multishell nanoparticles to carry identifiable codes in the time domain to quantitatively realize cancer diagnostics in living mice, which outperforms conventional methods. Temporal coding also enables deciphering through a scattering medium, as shown in the $NaYF_4$:Yb/Er@$NaYbF_4$@$NaYF_4$@$NaYF_4$:Nd nanostructure. Here, the inert $NaYF_4$ interlayer impedes energy crosstalk from Nd^{3+} to Yb^{3+} under 808 nm excitation. Wavelength and lifetime binary encoding were also demonstrated. Tm^{3+}-sensitized nanoparticles with NIR-II excitation and emission provide a new transplantable multiplexing encoding perspective for *in vivo* deep-tissue imaging.

4. Emerging optical applications of ANPs

PA materials have unequivocally showcased their remarkable potential in the realm of optical applications. Their integration with targeted nanoplatforms has further solidified the vast prospects of photon upconversion in nanophotonics. This section delves into noteworthy advancements in luminescence thermometry, ANP-based lasers, mesmerizing full-color 3D volumetric displays, cutting-edge information storage techniques, impregnable information security measures, and innovative anti-counterfeiting solutions—these groundbreaking developments offer fresh perspectives and unveil exciting possibilities in the realm of emerging photonic applications.

4.1. Luminescence thermometry

Temperature, a fundamental property in various scientific disciplines, often necessitates reliable thermometers for accurate monitoring.[120,121] The development of effective thermometers is crucial, particularly in challenging environments characterized by aggressive media composition, electromagnetic interference, limited access, or compact size.[122,123] Luminescent probes have emerged as a promising approach for meeting

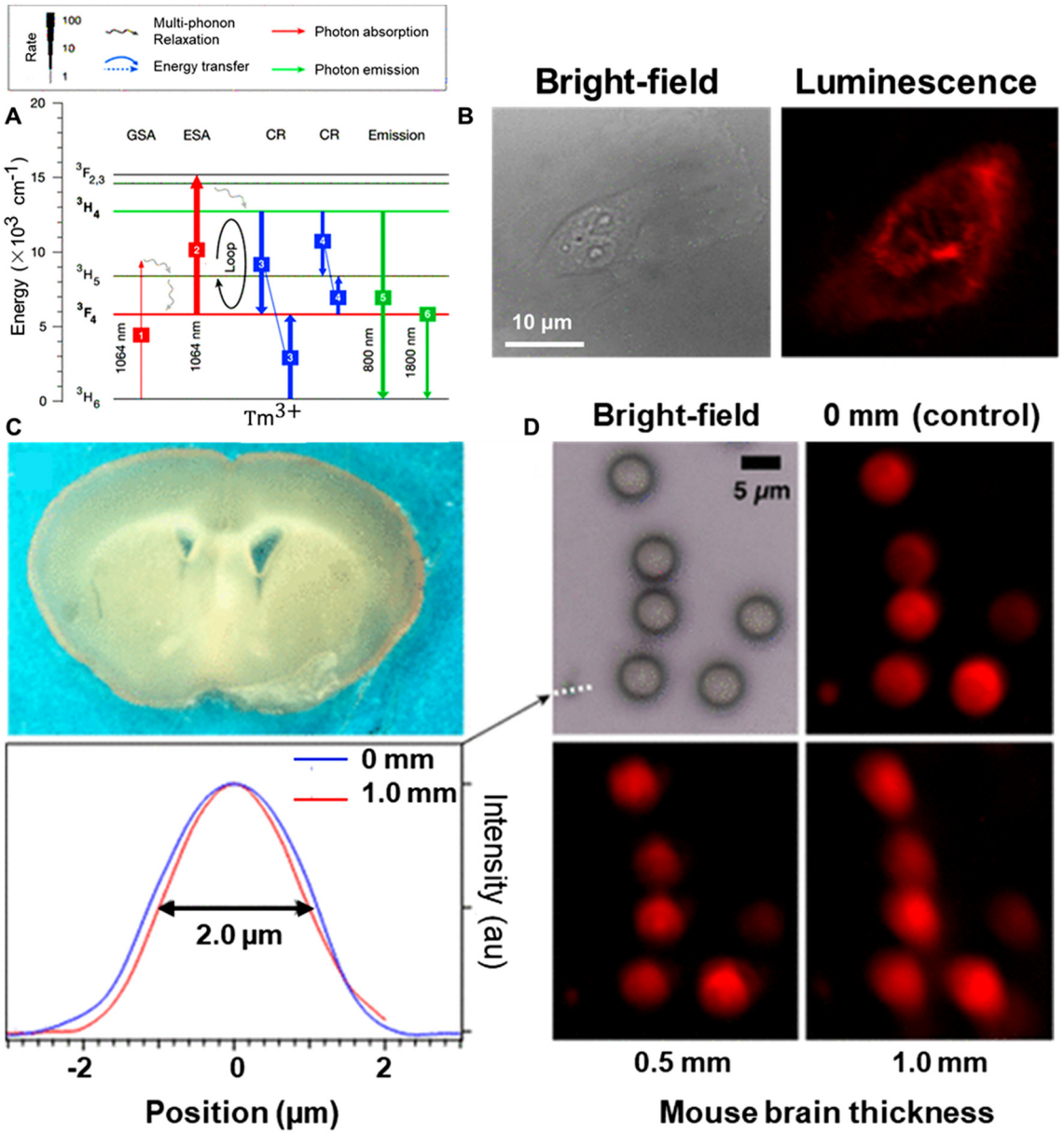

Fig. 15 Application of ELNPs in deep-tissue imaging. (A) A proposed looping mechanism of Tm^{3+}-doped $NaYF_4$ emitting 800 nm upon 1064 nm (10^5 W cm^{-2}) non-resonant photoexcitation. (B) Confocal imaging of live HeLa cells after treatment with 1.5% Tm^{3+} ELNPs. Bright-field (left), luminescence integrated between 740 nm and 870 nm (right). (C and D) Deep-tissue imaging of mouse brain slice through ELNPs. Representative mouse brain slice through which ELNP beads were imaged (C). Bright-field and confocal luminescence images of Tm^{3+}-doped ELNP beads imaged through 0, 0.5, and 1 mm-thick brain slices upon 1064 nm excitation (10^6 W cm^{-2}) (D). Reproduced with permission from ref. 37. Copyright 2016, American Chemical Society.

these requirements, as they enable temperature measurements without the need for direct contact and can operate in diverse chemical environments. In luminescence thermometry, a well-recognized parameter is relative sensitivity (S_R), which is quantified using the following formula:

$$S_R = \Delta\lambda/\Delta T \times 1/\lambda \quad (2)$$

Here, $\Delta\lambda$ represents the change of wavelength of the luminescent probe per temperature interval ΔT, λ denotes the initial wavelength, and Relative sensitivity provides an essential measure of the probe's responsiveness to temperature variations.

Several fluorescent materials have been employed in luminescence thermometry, including organic fluorescent dyes, polymer compounds, quantum dots, carbon nano-structures, and conventional lanthanide-doped inorganic nano/or micro materials.[124–129] Of these, lanthanide-doped ANPs are among the most likely candidates for thermal sensing owing to their enormous optical nonlinearity with low excitation power, non-contact measurement, compatibility with different

chemical environments, and the ability to monitor temperature remotely. These attributes make ANP-based thermometers particularly useful in applications where direct physical contact is impractical or undesirable.[5] However, the complexity introduced by the PA process complicates measurement and interpretation compared with traditional techniques *i.e.* simple luminescence intensity ratio (LIR), demanding sophisticated instrumentation and data analysis methods. ANP-based temperature sensing is also susceptible to influences beyond temperature, such as excitation intensity and nanoparticle aggregation, potentially undermining measurement accuracy. Moreover, the narrow operating range and sensitivity dependence on temperature may limit ANPs' suitability for niche applications where stability and reproducibility are paramount. Addressing these challenges requires robust calibration methods, improved nanoparticle stability, integration with advanced data analysis techniques, and exploration of alternative sensing strategies.[8] Despite these hurdles, ANPs hold promise for revolutionizing temperature sensing in diverse applications, driving ongoing research efforts to overcome their limitations.

In recent times, different methodologies have been developed for the temperature readout process or 2D/3D mapping including the absolute intensity of a single emission band (ABS), the ratio of single band emission intensity excited with two wavelengths (SBR)/or the ratio of two excited bands obtained using single emission band (EIR), and the ratio of two luminescent intensities obtain using one excitation wavelength (LIR)[130–134] Fig. 16. These methodologies focus on the luminescence of a pair of energetically connected levels which are closely spaced with an energy difference below 2000 cm^{-1}. This proximity ensures a strong likelihood of nonradiative transitions between the two levels. Additionally, the higher energy level must display a significantly higher emission intensity compared with the background noise within the relevant temperature range.

In the field of luminescence nano thermometry, Marciniak *et al.* presented the first study utilizing the pre-avalanche energy looping-like behavior in Nd^{3+} ions doped nanomaterials such as $NaYF_4$, Y_2O_3, $YGdO_3$, $YAlO_3$, $Y_3Al_5O_{12}$, $LiLaP_4O_{12}$, and Gd_2O_3 under non-resonant 1064 nm NIR photoexcitation for luminescence thermometry.[135] Because of the energy looping amplification process, the observed avalanche-like NIR emission at 808 nm was very strong, which the authors emphasized by describing it as room temperature avalanche-like behavior. It was demonstrated that this excitation method exhibits a threshold value of excitation power and temperature. The authors explained that the first excited level from which the ESA occurs exhibits thermal coupling to the ground level according to the Boltzmann distribution rule, despite the energy distance between them reaching as high as 1900 cm^{-1}. However, even despite the very small population of this level, the amplification processes occurring, in this case, were related to the occurrence of CR from $^4F_{3/2}$, $^4I_{9/2} \leftrightarrow {}^4I_{15/2}$, $^4I_{15/2}$ transition. Consequently, this contributed jointly with non-radiative multi-phonon relaxation from the higher $^4I_{15/2}$, and $^4I_{13/2}$ levels to increase the occupancy of the $^4I_{11/2}$ level, and thus the observed emission was recordable even at low temperatures. As the temperature rose, there was an observed augmentation in the emission intensity of the Nd^{3+} ions, allowing them to reach an S_R above 5% K^{-1} at temperatures below 325 K. Interestingly, for the various materials tested, a correlation between the S_R (at 310 K) and the minimum energy gap between the sublevels of the ground- and $^4I_{11/2}$ states was

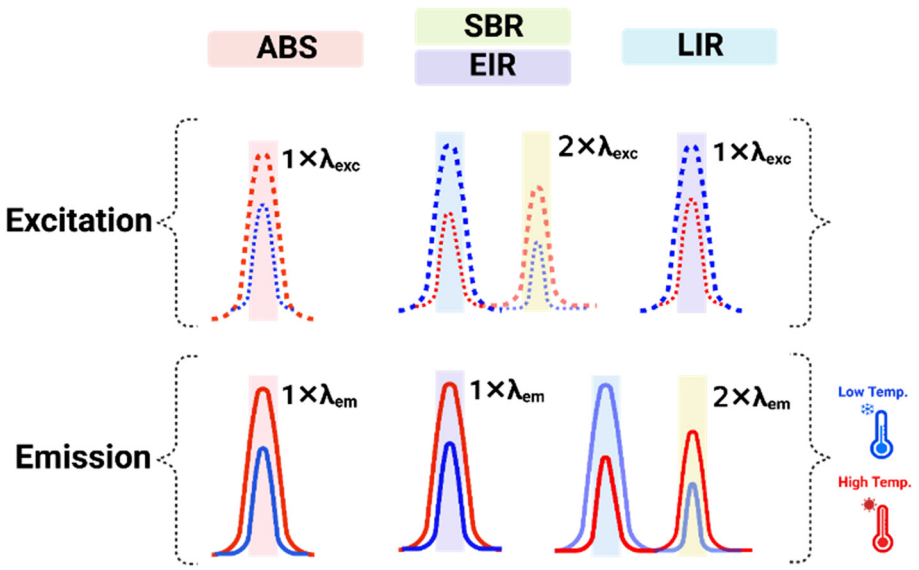

Fig. 16 Methods applied in luminescence thermometry to measure the temperature: ABS = absolute intensity of a single emission ban, SBR = ratio of the intensity of a single emission band excited with two wavelengths/or EIR = ratio of the intensity of two excitation bands obtained when monitoring a single emission band, and LIR = ratio of the intensity of two emission bands obtained using a single excitation wavelength.

detected. A theoretical model of the system of rate equations was also presented, which predicted the thermal dependence of the rise times observed in this type of system. Based on this, a unique measurement method was proposed to study the half-time before the saturation intensity was reached. It was shown that this parameter is a function of temperature and that the implementation of a method to measure it can be very uncomplicated and inexpensive. Since the best results were achieved for $LiLaP_4O_{12}$:Nd^{3+}, it was concluded that together with the proposed novel measurement method, it is a promising phosphor for spot measurements or temperature mapping for applications in biological conditions.

Another publication also reporting energy-looping behavior using the Single emission band intensity ratio (SBR) methodology was presented by Trejgis *et al.*, who reported SBR-type thermometer-based Nd^{3+}-doped $LaPO_4$ nanoparticles for the first time.[136] Both the excitation and the emission in this experiment were under the NIR region. This was an extension of the sole earlier paper on pre-avalanche energy looping-based thermometry using Nd^{3+} ions, which was presented by Marciniak *et al.*;[135] however, in that case, only the absolute intensity of a single band emission was analyzed. But, in this work, the authors described the use of two excitation wavelengths at 808 nm and 1064 nm, matching the GSA associated with the $^4I_{9/2} \rightarrow {}^4F_{5/2}$ transition and the ESA associated with the $^4I_{11/2} \rightarrow {}^4F_{3/2}$ transition, respectively. The experiment revealed a thermally activated enhancement in luminescence intensity at around 890 nm with excitation matching the GSA. Similarly, a thermal increase in intensity was observed at 1064 nm with non-resonant ESA. Transitions from higher emissive levels thermally coupled to the $^4F_{3/2}$ level were also observed above certain temperatures. Significant enhancement in emission intensity gain was recorded for all ESA-excited emission bands, particularly with higher concentrations of Nd^{3+} ions due to CR effects. The study achieved a high sensitivity ratio (SR) reaching up to 7% K^{-1} at 303 K using the SBR approach, which decreased with increasing temperature. Another method presented achieved an SR higher than 2% K^{-1}, involving monitoring two different bands using two different excitations. By combining these methods, an SR higher than 2% K^{-1} was demonstrated for the entire temperature range studied (273 K to 573 K).

In a recent study, Korczak *et al.* experimentally investigated the impact of temperature (−175 °C to 175 °C) on 15% Yb^{3+}/0.5% Pr^{3+} co-doped $NaYF_4$ core/shell ANPs,[5] emitting light at 607 nm and 482 nm corresponding to transitions from the $^3P_0 \rightarrow {}^3H_6$ and $^3P_0 \rightarrow {}^3H_4$, respectively, under 852 nm pumping wavelength at an intensity of 1.5 mW cm^{-2} Fig. 17(A). Unlike in those previous SBR-based thermometry studies, the authors demonstrated that all the significant variations of the PA nonlinearity (S = 4.5–9), PA gain (from 50 up to 175), and PA threshold (from 100 to 700 kW cm^{-2}) were observed under temperature rise from −175 °C to 175 °C, respectively Fig. 17 (B). This approach assured relative temperature sensitivity above 0.5% $°C^{-1}$. Simultaneously, with increasing temperature, the emission intensity at 482 nm and 607 nm decreased significantly up to four orders of magnitude for selected excitation powers. Based on such substantial variations in the intensity of a particular emission band, the corresponding temperature relative sensitivity was calculated and the maximum value of 7.5% $°C^{-1}$ was obtained at 0 °C. These relationships not only confirm the suitability of such an approach for luminescence thermometry but also evidence a complex set of coexisting phenomena that drive PA emission. The presented results not only enhance knowledge of fundamental mechanisms and the sensitivity of the sensitized PA emission to temperature changes but also show the possibility of using PA materials as sensitive nanothermometers. Besides this prediction, temperature also affects the internal processes that occur within and between dopant ions in PA behavior. For the proof of concept, Szalkowski *et al.* predicted the impact of temperature on energy gap-dependent multi-phonon relaxation and inter-ionic energy transfer processes in PA behavior in Tm^{3+}-doped $NaYF_4$ ANPs.[137] Based on the DRE simulation results, significant sensitivity of PA emission to temperature was found with relative temperature sensitivities around 40% K^{-1} above 375 K, which additionally was dependent on excitation intensity. Furthermore, when the temperature dependencies of the specific processes contributing to the PA effect were eliminated, the researchers discovered that the temperature dependence of the multi-phonon relaxation from the intermediate $^3F_4$ state to the ground state played the most significant role in driving the simulated temperature dependence of PA emission. This process was observed to have a greater impact compared to the temperature dependencies of energy looping and non-resonant absorption, which is phonon-assisted in a ground state.

Luz *et al.* explored the behavior of $NdAl_3(BO_3)_4$ particles and investigated the possibility of optical switching within a PA mechanism using an auxiliary beam at 808 nm.[6] Initially, the particles were subjected to non-resonant ESA by a 1064 nm excitation laser beam with an excitation power intensity of 1.5 W, which was below the threshold power for excitation. Interestingly, they observed a significant increase in photoluminescence at a specific excitation threshold power, indicating the onset of a PA-like phenomenon. To further explore this behavior, the authors activated the auxiliary beam at 808 nm to optically switch the PA-like mechanism associated with the 1064 nm excitation. Remarkably, they observed a sudden onset of intense emissions at shorter wavelengths (690 nm, 660 nm, 600 nm) when the power intensity of the 808 nm beam was increased from 10 mW to 120 mW. This phenomenon was attributed to an increase in the population of the $^4I_{11/2}$ level within the particles. This population increase was facilitated by processes such as phonon emission ($^4F_{5/2}$, $^2H_{9/2} \rightarrow {}^4F_{3/2}$), multi-phonon relaxations ($^4F_{3/2} \rightarrow {}^4I_{15/2}$), and CR between two Nd^{3+} ions ($^4F_{3/2}$, $^4I_{9/2} \rightarrow {}^4I_{15/2}$, $^4I_{15/2}$). Furthermore, the auxiliary beam served as an additional heating source, raising the temperature of the particles beyond what was achieved by solely exciting the Nd^{3+} ions at 1064 nm Fig. 17(C and D). This additional heating contributed to the observed behavior, indicating a complex interplay between optical excitation, popu-

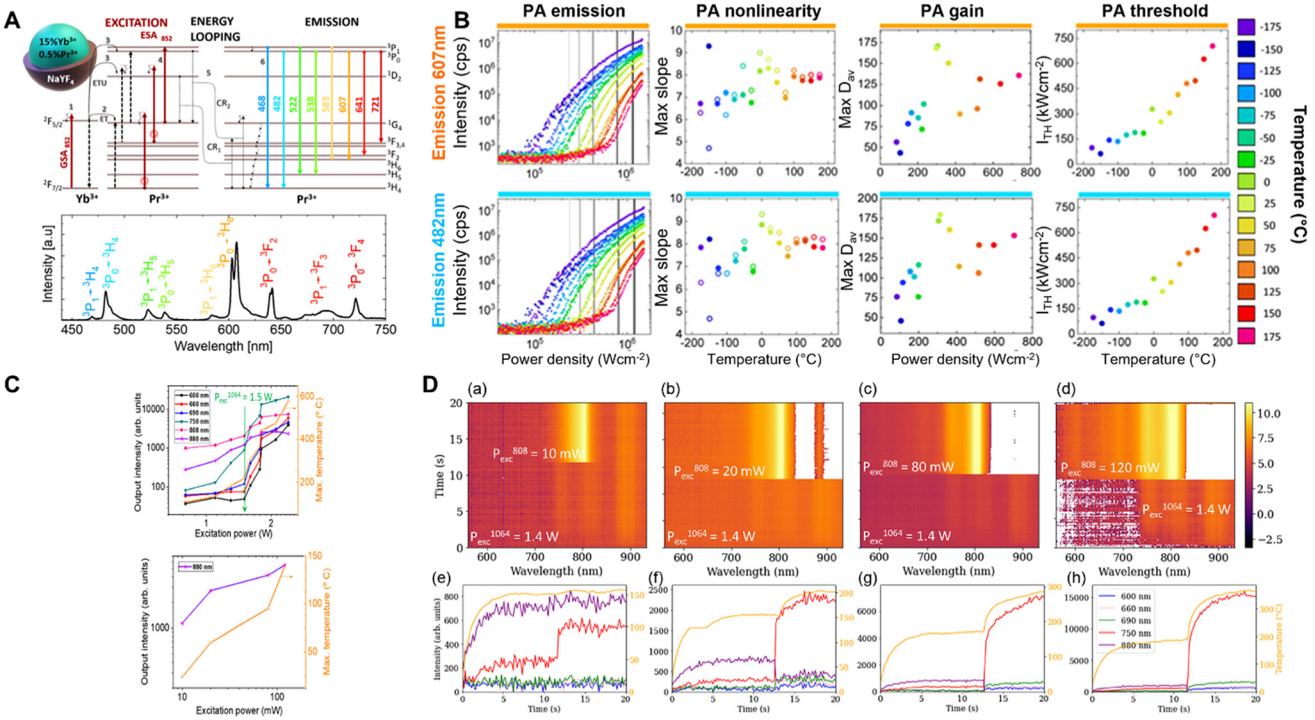

Fig. 17 ANPs in luminescence thermometry. (A) A proposed PA mechanism of core–shell avalanching nanoparticles under 852 non-resonant photoexcitation at room temperature (top) and their emission spectra at different emitting wavelengths corresponding to their transition states (bottom). Radiative and nonradiative transitions are indicated by solid and dotted lines, respectively. Multi-phonon relaxation procedures or phonon-assisted energy transfer processes are indicated by wavy arrows. (B) Temperature, and power-dependence characterization of the PA emission in $NaYF_4$:15%Yb^{3+},0.5%Pr^{3+}@$NaYF_4$ under 852 nm excitation. The top and bottom rows correspond to the orange color emission band at 607 nm and the blue color emission band at 482 nm, respectively, and reveal pump power dependence of PA emission intensity for various temperatures, the highest PA nonlinearities (S = 4.5–9), maximal PA gain at the excitation intensity corresponding to the highest nonlinearity, as well as demonstrate PA threshold at various temperatures. Reproduced with permission from ref. 5. Copyright 2023, AIP Publishing. (C) Excitation power-dependent luminescence of $NdAl_3(BO_3)_4$ photoswitched ANPs under non-resonant excitation at 1064 nm (left) and under resonant excitation at 808 nm, respectively. (D) Optical switching on the PA-like mechanism by the auxiliary beam at 808 nm with different excitation power intensities 10 mW (A), 20 mW (B), 80 mW (C), and 120 mW (D) exhibiting the emergence of strong emissions which characterizes the onset of the PA-like mechanism (Top) boosting the phonon emissions in the relaxation pathways of the Nd^{3+}, which is consistent with the particle temperature increase after excitation at 808 nm (right). Reproduced with permission from ref. 6. Copyright 2023, Optica Publishing Group.

lation dynamics, and temperature effects within the particles. This study is of fundamental importance for understanding PA phenomena and has potential applications in optical thermometry,[128] and light-to-heat conversion as nano heaters.[138]

4.2. ANP-based lasers

Laser technology has permeated diverse domains, spanning data storage, remote sensing, disease therapeutics, and photochemical processes.[139] The core principle of laser operation lies in the amplification of light through stimulated emission of radiation, necessitating an active medium consisting of a collection of atoms, molecules, or ions that are capable of amplifying light waves, a pumping source to establish population inversion, and optical resonators. Recent studies in crystal growth and nanoscale manipulation have advanced the fundamental principle of stimulated emission to new horizons. Crystal growth advancements have paved the way for a plethora of lasers made from solid-state materials to provide substitutes for conventional gas and liquid lasers. These solid-state lasers, developed since the 1980s, emit light across the near-UV, Vis, and NIR spectra. Of particular interest is deep-ultraviolet (deep-UV) diode lasing, which holds promise in precision engineering and biomedical applications. Successful deep-UV diode lasing relies on high-quality multilayer crystals within virtually defect-free lattices.[140–142] Earlier, optically lasers were assembled with bulk crystals doped with Ln^{3+} ions, boasting advantages such as longer lifetimes, high power output and efficiency, and impressive stability. However, they do come with inherent drawbacks. Their typically large and heavy design poses challenges in terms of portability and integration into compact devices. Managing thermal effects due to heat generation during operation adds complexity and cost to laser systems. Additionally, the fabrication of high-quality bulk crystals with precise optical properties can be both challenging and costly.[143–145] To address these challenges, researchers have turned their attention to developing Ln^{3+}-doped upconversion nanoscale-based lasers. However, the low quantum yield of traditional UCNPs and the challenges posed by 4–5 photon

upconversion transitions have hindered the exploitation of their full potential. Additionally, operating UC lasers at room temperature raises the possibility of depopulating the higher excited states, which encourages ESA and reduces the possible population inversion required for laser action.[146–148]

Significant attention has been directed toward photon-avalanching nanomaterials in advanced laser technology to overcome these limitations. Unlike bulk crystals, ANPs exhibit exceptional versatility and miniaturization potential due to their nanoscale size, enabling integration into compact and portable devices for a wide range of applications. Their unique ability to generate extreme nonlinear upconverted emission in visible or ultraviolet light under miniature pumping NIR laser sources offers unparalleled flexibility in light manipulation and photonics. Moreover, ANPs can be precisely engineered to achieve tunable optical properties, including emission wavelength, intensity, and coherence, allowing for customized laser designs tailored to specific applications.[8,35] Achieving population inversion in these materials enables the generation of a wide range of stimulated radiation when an optical cavity provides positive feedback against losses. Through designing specialized laser cavities and implementing suitable pump schemes, lasers based on photon-avalanching nanomaterials have been realized using both pulse and continuous-wave pumping methods, notably the avalanche-like energy looping mechanism in ANPs, resulting in bio-integrable, solution-processed CW upconverting nano or microlasers. These nanomaterial-based lasers exhibit higher efficiency and lower thresholds compared with traditional lasers, demanding less energy for operation while producing more intense light. As a result, they hold immense promise for applications spanning super-resolution microscopy, photodynamic therapy, chemical sensing, optical data storage, and more, spanning a broad range of wavelengths, from deep UV to NIR.[2]

In recent studies, two research groups, Fernandez-Bravo *et al.* and Liu *et al.* have investigated the use of energy-looping Tm^{3+}-doped nanoparticles (ELNPs) as an active medium in microcavities for achieving low-threshold CW lasing.[149,150] Fernandez-Bravo *et al.* designed stand-alone laser microcavities fabricated from 5 μm polystyrene (PS) microspheres known for host whispering gallery mode (WGM) refers to optical resonances that occur when light waves are confined within a microsphere due to total internal reflection, allowing them to circulate along the inner surface in a closed-loop path.[149] By coupling ELNPs to the WGM of the PS microsphere, stable lasing for over 5 hours could simultaneously achieve blue-colored visible and NIR emissions at 450 nm and 800 nm, respectively, at thresholds as low as 14 kW cm^{-2}; excited non-resonantly at 1064 nm, the ELNPs circumvented the potential optical and thermal damage typically associated with operational conditions. By leveraging an avalanche-like energy-looping mechanism, they effectively overcame these challenges and achieved population inversion more efficiently compared with conventional UCNPs, which is crucial for achieving lasing. The microcavities housing the ELNPs exhibited remarkable robustness, showing no signs of damage or deterioration under normal operational conditions. Moreover, the ability to generate CW lasing in microcavities submerged in blood serum highlights the promising practical applications of these microlasers for tasks such as sensing and illuminating intricate biological structures.[147]

Similarly, Liu *et al.* utilized 5 μm PS-WGM microcavity coated with a sub-monolayer of 15.8 nm Tm^{3+}-doped ELNPs, revealing their potential as an active medium for low-threshold micron-sized laser.[150] The coupled ELNP-PS microresonators effectively reduced the background spontaneous emission and exhibited anti-Stokes lasing at 800 nm with a low threshold (1.7 ± 0.7 kW cm^{-2}) when excited by CW radiation at 1064 nm. Compared with single ENLP-PS microsphere cavities that only exhibited spontaneous emission, the use of the WGM microresonator led to improved lasing performance. The relationship between nanoparticle deposition, physical morphology, and lasing quality was demonstrated, showing a 25-fold reduction in average lasing threshold distributed over a 30-fold narrow power range for ELNPs-PS microresonator. The use of a 1064 nm CW excitation laser source minimized thermal damage and allowed for stable and biocompatible microcavities, making them suitable for biological applications such as tissue tracking analysis through the imaging of microlasers using phantoms that mimic the scattering properties of biological tissue. The submonolayer-coated, 5 μm ELNP microlasers exhibited distinct WGM lasing even when pumped through a 1 mm-thick phantom composed of 1% w/v agarose and 0.25% w/v intralipid. Although the scattering of both excitation and emitted light by the phantom resulted in an overall 8-fold reduction in microlaser intensity compared with imaging without the phantom Fig. 18(A), the fact that the submonolayer-coated microlasers still achieved CW lasing in such scattering conditions underscores their significantly lower thresholds compared with previously reported conventional UCNP or fiber-based microlasers. These findings offer promising prospects for various applications, particularly in the fields of imaging, sensing, and optical manipulation. The enhanced performance, robustness, and compatibility with biological samples make these energy-looping lasers valuable tools for investigating complex biological structures and environments. Further exploration and optimization of these systems could lead to advancements in the development of highly efficient energy-looping lasers and their widespread application in diverse scientific and technological domains.

Shang *et al.* focused on achieving exceptionally low threshold lasing emissions within a microcavity laser.[7] They achieved this by effectively controlling CR processes, which enabled the establishment of population inversion at the intermediate state of the $^3H_4$ level in single Tm^{3+}-doped nanoparticles utilized as the gain medium. To accomplish this, the researchers optimized the concentration of Tm^{3+} ions and applied a single-layer coating of self-assembled nanoparticles onto the microcavity, which had a diameter of around 5 μm. This coating minimized scattering loss and facilitated the efficient generation of lasing emissions. Remarkably, they successfully achieved lasing emissions at approximately 802 nm

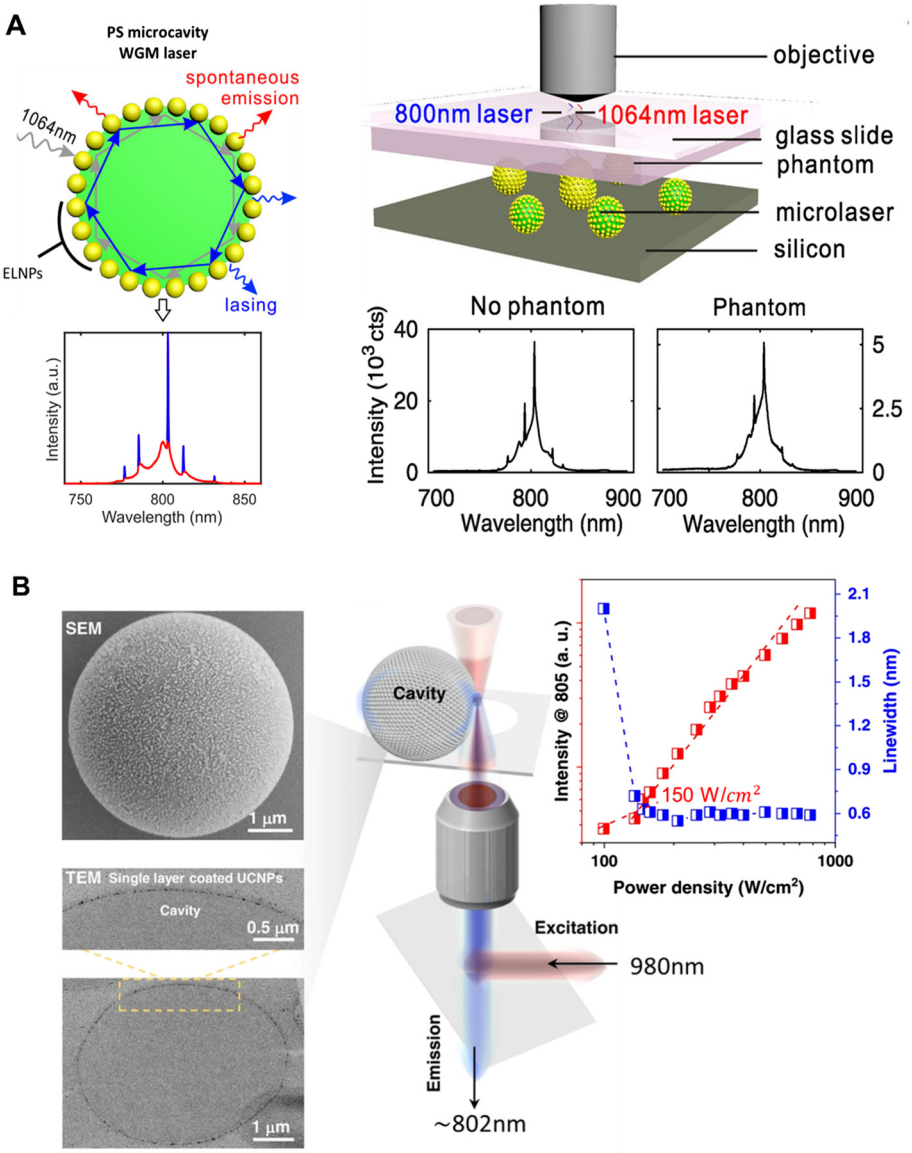

Fig. 18 Towards ANP-based lasers. (A) Cartoon image of ELNPs coated-PS microcavity illustrating low-threshold WGM lasing at 800 nm upon 1064 nm excitation, resulting in reduced spontaneous emission (left), the imaging of five microlasers located within scattering media was conducted using focused 1064 nm light at an intensity of 1700 kW cm^{-2}, achieved by an objective lens. The microlasers were excited through a phantom composed of 1% agarose and 0.25% intralipid, while the emitted light at 800 nm was collected through the same objective lens (Right). Additionally, the WGM spectrum of a single microlaser was obtained both with and without the presence of a 1 mm-thick phantom (right and left, respectively). Reproduced with permission from ref. 150. (B) SEM and TEM images of a 5 μm PS-microcavity coated with a monolayer of self-assembled UCNPs showing the distribution of nanoparticles on the surface (left) and the proposed imaging system showing excitation and lasing with an ultra-low threshold at 150 W cm^{-2} (right). Reproduced with permission from ref. 7. Copyright 2022, Springer Nature.

with an impressively low threshold of around 0.15 kW cm^{-2} (equivalent to 150 W cm^{-2}) at room temperature Fig. 18(B). This threshold was nearly two orders of magnitude lower than those reported in previous studies by Fernandez-Bravo *et al.*[149] and Liu *et al.*[150] These findings highlight the significant potential of nanoparticles with adjustable concentrations as highly efficient gain materials for room temperature CW lasers on both the microscale and nanoscale. The ability to achieve such low thresholds opens up exciting possibilities for various practical applications, including intracellular tagging and imaging. By addressing the challenges associated with threshold levels, this study contributes valuable insights to the development of highly efficient and practical laser systems at the micro and nanoscale. Despite these advantages, stability remains a challenge for ANP-based lasers. To address this, future research efforts could focus on surface modification techniques to enhance ANP stability, such as coating with biocompatible polymers or inorganic shells. Additionally, controlled synthesis methods and purification techniques can be employed to ensure uniformity and minimize defects in ANP

structures. By overcoming stability challenges, ANPs hold immense promise for advancing laser technology, opening new avenues for high-performance and versatile light sources in various applications.

4.3. Optical data storage and information security

Full-color tuning refers to the ability to control the lifetime (duration) of the emission of light in different colors (wavelengths) emitted by a material. Full-color lifetime tuning is important in applications such as displays and lighting; the capacity to regulate the hue and duration of emitted light can significantly impact the quality of the visual experience. While achieving full-color lifetime tuning requires precise design and synthesis of materials concerning their chemical structure and properties, variations in composition, phase, and structure offer a valuable approach for producing a diverse range of emission colors. However, controlling the color gamut within a material of fixed composition remains a formidable task. The parity forbidden 4f–4f transition property of lanthanide ions qualifies them with decay times from microseconds to milliseconds, which are substantially longer as compared with molecular dyes and QDs. This feature makes it more easily distinguished from the background or noise signal. The upconversion luminescence lifetimes can be tuned by artificially manipulating energy transfer processes between lanthanide ions or interparticles. For instance, Tm^{3+}-doped nanoparticles with distinct lifetimes can be created by controlling CR occurring at the blue-emitting $^1G_4$ level. A gradient doping strategy was proposed to realize the independent control of upconversion emission intensity and lifetime by manipulating the excitation energy dynamics.[151,152] Minimizing surface quenching also results in the lifetime tuning from 33 μs to 2.2.[153] The migration-mediated multi-shell nanostructure becomes an intelligent platform for controlling lifetime by manipulating the energy transport channels.[154]

Revolutionizing the realm of 3D displays, avalanching optical materials have emerged as a focal point due to the remarkable emission bands and unwavering stability of lanthanide ions. A significant advancement has been made in achieving full-color observation using core–multishell nanostructures. Deng *et al.* presented an innovative and versatile method to dynamically tune the emission of core–multishell nanoparticles by varying the pulse width of a 980 nm NIR laser beam.[155] This groundbreaking approach allows for the creation of full-color 3D display systems with high spatial resolution, offering localized control over the color gamut through nanoparticles dispersed in Polydimethylsiloxane (PDMS) fiber, facilitated by a non-steady-state UC process. The researchers discovered that by adjusting the pulse duration of the excitation laser, they could control the energy transfer between dopant ions in a core/shell nanostructure. Increasing the pulse duration from 0.2 ms to 6 ms at 980 nm enabled continuous modulation of the intensity ratio between green and red emission from the shell, co-doped with Ho^{3+}/Ce^{3+} ions. This modulation was achieved through a CR process involving Ho^{3+} and Ce^{3+} ions. Furthermore, the Tm^{3+}-containing core exhibited blue emissions at 475 nm when excited by an 808 nm continuous-wave laser through the energy transfer pathway of $Nd^{3+} \rightarrow Yb^{3+} \rightarrow Tm^{3+}$, with a high concentration of Nd^{3+}. The experimental results highlighted the crucial role played by non-steady states in governing the excitation dynamics and luminescence emission of nanoparticles, distinct from traditional photon upconversion under steady-state processes. Using a multilayer core–shell design and skillful regulation of CR and energy migration pathways, the researchers successfully achieved tunable emission, resulting in a wide array of arbitrary colors and paving the way for full-color volumetric three-dimensional displays created from nanocrystals of consistent composition. This landmark study represents a significant step toward precise control of color emission and opens up promising possibilities for various applications in optical memory, security printing, and other unexplored realms.

ANPs have also emerged as a promising technology with immense potential in the field of optical storage. By incorporating these nanoparticles as active elements within the storage medium, significant advancements in data storage density and retrieval speed can be achieved. This remarkable approach allows for the storage and retrieval of data using light pulses at substantially higher densities and faster rates compared with conventional storage methods. One major advantage of ANPs in optical storage is the ability to achieve high storage density. With ANPs serving as the key components, data can be packed more densely, enabling the storage of larger amounts of information within a smaller physical space. This increased storage density is crucial in the era of big data and information-intensive applications.

Another advantage lies in the potential for rewritable and multi-level optical storage. ANPs offer a wide range of color tunability, allowing for versatile encoding and storage of data. By manipulating the composition and size of the nanoparticles, diverse emission wavelengths can be achieved, enabling multi-level storage and significantly expanding the data capacity. For the proof of concept, Lu *et al.* successfully demonstrated precise control over the UC lifetime of $NaYF_4$ nanocrystals doped with Yb^{3+} and Tm^{3+} ions by manipulating the CR process with varying concentrations of blue-emitting Tm^{3+} ions.[151] Through this manipulation, the researchers achieved a wide range of UC lifetimes, from 25.6 μs to 662.4 μs, within a single blue emission band. This groundbreaking achievement led to the development of a collection of Tm^{3+}-doped τ-dots with tunable lifetimes, allowing for optical multiplexing with over 10 000 distinguishable codes. By combining different codes based on color, intensity, and lifetime, researchers were able to leverage luminescence as a potent analytical technique, particularly valuable in life sciences and medicine. This advancement opens up new possibilities for diagnostic and analytical applications by addressing the complexity of these fields. Furthermore, the controlled manipulation of upconversion lifetimes in nanocrystals opens exciting opportunities in high-density data storage. With the ability to encode information in the form of distinct lifetime codes, the potential for compactly storing vast amounts of data is greatly

expanded. This breakthrough paves the way for the development of advanced data storage systems with higher capacities and improved data retrieval capabilities.

Recently, Lee *et al.* reported an impressive development in NIR-photoswitchable ANPs doped with 8% Tm^{3+}, designed for optical data storage.[4] To explore their potential in high-density patterning applications, the researchers deposited a thick film of ANPs (~5 microns) onto a glass slide. These nanoparticles demonstrated the ability to alternate between darkened and brightened states, enabling the creation of sequential 2D and 3D patterns, which were visualized using conventional confocal microscopy. By utilizing CW 1064 nm and 700 nm laser beams, the team successfully created rewritable 2D patterns, where the 1064 nm beam was used for imaging and darkening, while the 700 nm beam enabled precise writing. The nonlinear PA emission and photodarkening properties of these ANPs allowed for ultra-high resolution patterning, achieving features smaller than 70 nm, with long-lasting storage lifetimes and unlimited read-write cycles. Additionally, due to the low scattering of NIR wavelengths, these nanoparticles facilitated subsurface imaging, enabling the optical patterning of complex 3D designs measuring approximately ~3 microns in all dimensions Fig. 19(A and B). This breakthrough opens new possibilities for ANPs in high-density optical memory and robust pat-

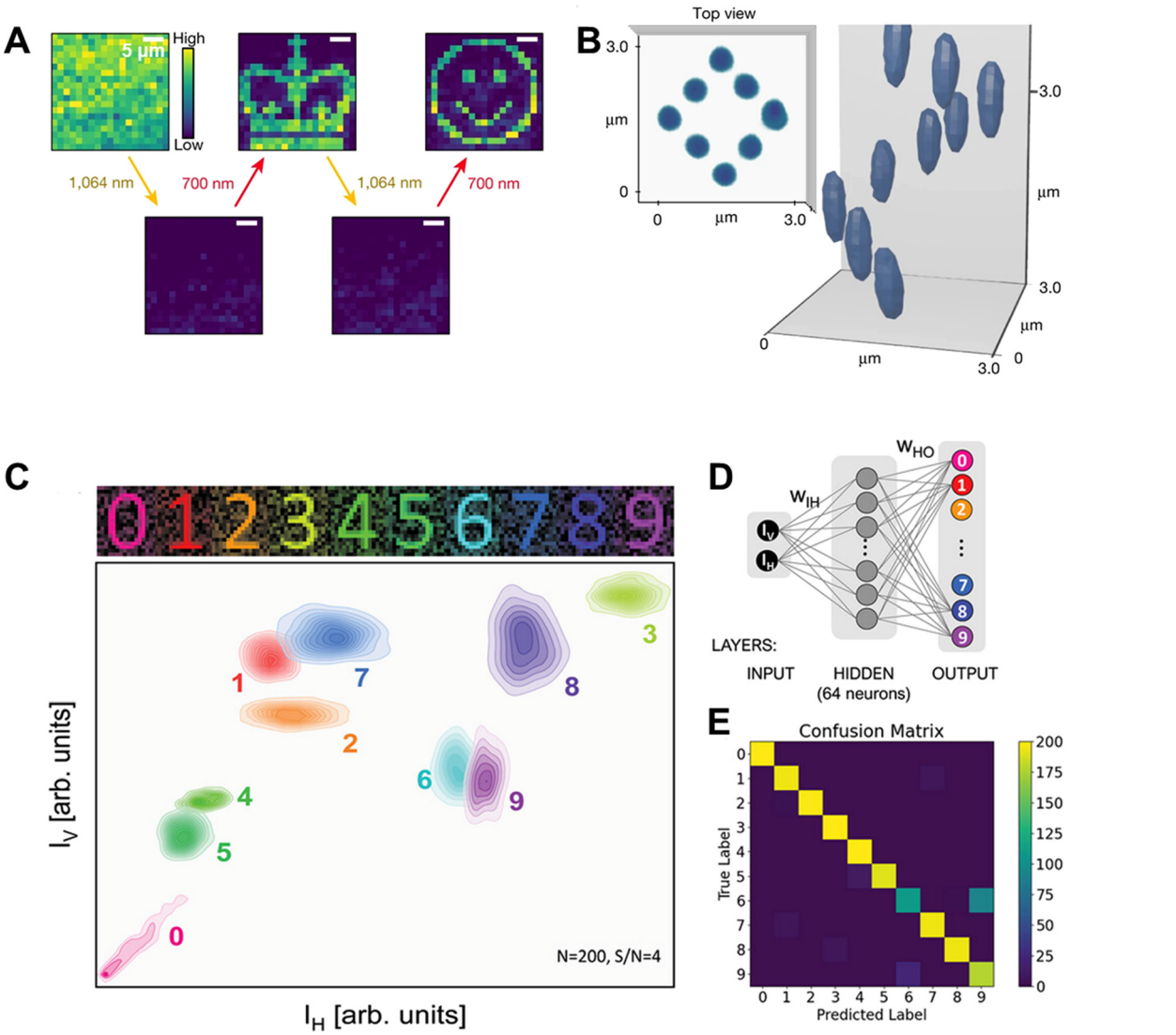

Fig. 19 ANPs in optical data storage. (A) Rewritable photopatterns of the crown and smile face on a 100 nm thick ANP film. (B) 3D images of diamond spiral patterned into a 5 micron-thick ANPs film. Reproduced with permission from ref. 4. Copyright 2023, Springer Nature. (C) A schematic representation of 2D histograms plotting the occurrences of horizontal (I_H) *versus* vertical (I_V) PA intensities facilitating feature extraction from noisy digit patterns (signal-to-noise ratio, S/N = 4) for digit signs "0" through "9". (D) The extracted I_H and I_V features from individual experiments served as input data for a simple artificial neural network (ANN). The network architecture consisted of a 2-neuron input layer, a 64-neuron hidden layer, and a 10-neuron output layer, enabling it to classify the digit signs effectively. (E) The performance of the ANN was evaluated using a confusion matrix, demonstrating successful digit classification with an impressive accuracy of 93%. Reproduced with permission from ref. 156. Copyright 2024, Wiley John and Sons.

terning applications in both 2D and 3D. In another significant study, Bednarkiewicz *et al.* demonstrated the use of ANPs as powerful tools for advancing all-optical neuromorphic computing.[156] These nanoparticles exhibited remarkable properties such as paired-pulse facilitation, short-term memory, and *in situ* plasticity, allowing them to emulate key behaviors of biological synapses. Their highly nonlinear threshold responses enabled efficient and selective signal amplification, mirroring the activity of neurons. Using these unique features, the researchers developed a two-input photonic neural network capable of performing tasks like 2D pattern recognition and feature extraction Fig. 19(C–E). These findings highlight the vast potential of ANPs in a range of cutting-edge technologies. For data storage, they offer precise, high-resolution patterning and long-term stability. In neuromorphic computing, they provide a pathway to biologically inspired, next-generation computing platforms that integrate advanced photonic systems for efficient data processing, adaptive control, and storage.

5. Current challenges and limitations of ANPs for frontier applications

In addition to the aforementioned emerging applications, ANPs possess unique optical properties that position them as promising candidates for several frontier applications, including optogenetics, optical sensing, and targeted drug delivery. However, significant challenges must be addressed to translate these promising materials into practical and widespread use. This section explores the key limitations in these areas and discusses potential strategies for overcoming these challenges.

5.1. Optogenetics

Optogenetics is a cutting-edge interdisciplinary field that combines techniques from optics and genetics to control and monitor the activity of individual neurons or specific neural circuits within living organisms. It utilizes light-sensitive probes, called opsins, to selectively modulate the electrical activity of neurons in response to light stimulation.[157,158] Lanthanide-doped ANPs may work as a remarkable light-sensitive probe, which may make them highly intriguing for optogenetics. These nanoparticles exhibit exceptional nonlinear upconverted emission in the visible or UV spectrum when exposed to a miniature pumping NIR laser source. This unique property holds immense potential for advancing optogenetics research, offering a novel avenue for precise manipulation of neuronal activity using light stimulation.[2,8] However, despite their promising potential, there are several reasons and challenges associated with the use of these ANPs in optogenetics.

Deep tissue penetration. One of the primary reasons for using ANPs in optogenetics is their ability to generate extreme luminescence in the UV-Vis region under NIR light. This property allows for deep tissue penetration, which is essential for stimulating or inhibiting neurons deep within the brain without causing damage to surrounding tissue. However, achieving sufficient penetration depth remains a challenge, particularly in the complex and heterogeneous environment of the brain. Innovative approaches for enhancing the penetration capabilities of ANPs are required. Developing ANPs with enhanced quantum yields and optimizing NIR laser parameters can improve signal strength. Advanced delivery systems, such as implantable optical fibers or waveguides, may also aid in overcoming depth limitations.

Biocompatibility. ANPs may be used effectively in optogenetics; however, they must be biocompatible to ensure minimal toxicity and immune response when introduced into living organisms. Although surface modification techniques can improve biocompatibility, maintaining the optical properties of ANPs while enhancing their biocompatibility is a significant hurdle. Also, exploring biodegradable coatings and biomimetic materials could improve compatibility, reduce immune responses, and enhance integration with neural tissues.

Targeting specific neuronal populations. Effective optogenetic applications demand precise targeting of specific neuronal populations. Functionalizing ANPs with targeting ligands can enhance cell-type specificity, but achieving reliable and spatially precise control over neuronal activity requires further optimization. Also, advancing ligand engineering, using multifunctional biomolecules, and employing AI-driven ligand screening could enhance targeting precision.

Delivery and distribution. Delivering ANPs to the target area within the brain and ensuring uniform distribution throughout the tissue is crucial for effective optogenetic modulation. Various delivery methods, such as direct injection or systemic administration, have been explored, each with its advantages and limitations. Overcoming barriers to efficient delivery and achieving homogeneous distribution of ANPs within the brain represent significant challenges in the field. However, developing novel carriers like liposomes, exosomes, or magnetic nanoparticles for localized delivery and leveraging microfluidic technologies for precise administration can address these issues.

Integration with optogenetic tools. The compatibility of ANPs with existing optogenetic tools such as opsins requires careful tuning of spectral properties. Designing ANPs with customizable spectral properties, improving their temporal response, and developing complementary imaging systems can facilitate seamless integration.

5.2. Optical sensing

In the field of optical sensing, ANPs may gain significant attention due to their unique properties, including stronger laser pump-induced ESA, clear excitation-power thresholds, sharp emission bands, long luminescence lifetimes, and excellent photostability. These characteristics make them promising candidates for various sensing applications.[159] However, several challenges must be addressed.

Sensitivity. One of the primary reasons for utilizing ANPs in optical sensing is their high sensitivity to changes in their local environment. ANPs can act as luminescent probes, with their emission intensity or lifetime being modulated by

analyte concentrations, pH, temperature, or other environmental parameters. However, achieving high sensitivity and selectivity for specific analytes while minimizing interference from background signals remains a challenge. However, implementing advanced functionalization techniques and employing ratiometric sensing strategies could enhance selectivity and accuracy.

Multiplexing capabilities. Multiplexed sensing offers significant advantages but requires a precise design to avoid crosstalk between different emission channels. However, leveraging machine learning algorithms for signal deconvolution and developing ANP sensor arrays with well-separated emission peaks can address multiplexing challenges.

Cost and scalability. Cost-effective synthesis methods and scalable production processes are essential for the widespread adoption of ANP-based sensors in research and commercial applications. Addressing challenges related to production costs, scalability, and reproducibility is crucial for overcoming barriers to large-scale manufacturing and market penetration of ANP-based sensing technologies. Investigating low-cost precursors, scalable synthesis methods, and batch-process optimizations may be essential for large-scale manufacturing.

5.3. Targeted drug delivery

The term "targeted drug delivery" refers to the process of delivering the correct dosage of the drug to a specific location in the body through a structured system. It encompasses the selection of a carrier, a delivery route, and a specific target site for the drug to act upon.[160,161] The remarkable nonlinear properties and tunable surface chemistry of lanthanide-based ANPs can show significant interest for visualizing drug delivery. However, several reasons and challenges exist in utilizing ANPs for drug delivery.

Targeted delivery. ANPs can be functionalized with targeting ligands, such as antibodies or peptides, to achieve targeted delivery of therapeutic agents to specific cells or tissues. This targeted approach can enhance drug efficacy while minimizing off-target effects and systemic toxicity. However, achieving selective binding and uptake by target cells remains a challenge, particularly in complex biological environments with heterogeneous cell populations. To address this, multi-modal ANPs could be developed with combinatorial targeting strategies (*e.g.*, integrating antibodies, and aptamers) that could improve selectivity.

Controlled release. The controlled release of therapeutic payloads from ANPs is crucial for achieving desired pharmacokinetics and minimizing side effects. Various stimuli-responsive systems, such as pH, temperature, light, or enzyme-sensitive linkers, have been investigated to achieve spatiotemporal control over drug release from ANPs. However, optimizing the release kinetics, achieving precise control over release profiles, and ensuring payload stability during storage and delivery are ongoing challenges in ANP-based drug delivery systems. However, utilizing hybrid nanoparticles that respond to multiple stimuli and incorporating precision-release mechanisms like photoactivation may enhance therapeutic outcomes.

Scale-up and manufacturing. Developing scalable synthesis methods for ANPs is essential for their practical implementation in drug delivery applications. Challenges related to batch-to-batch reproducibility, cost-effectiveness, and quality control need to be addressed to enable large-scale production of NP-based drug delivery systems for clinical use. However, exploring continuous flow reactors and modular synthesis platforms could enable high-quality production at scale.

Regulatory approval. The long-term toxicity and biocompatibility of ANPs are critical concerns for clinical translation. Standardizing safety evaluation protocols, conducting extensive preclinical studies, and fostering collaborations with regulatory agencies will be pivotal in overcoming these barriers.

6. Conclusion and future prospects

ANPs have experienced remarkable breakthroughs in recent years, with significant progress in mechanistic understanding and frontier applications. ANPs possess valuable on-demand properties, accessible through the design and tunable characteristics of their nanostructure and external stimuli, presenting exciting prospects for various applications in nanophotonics. These applications encompass ANP-based lasers, luminescent thermometry, 3D displays, optical storage, and information security. Moreover, ANPs have demonstrated their potential in biological imaging, offering highly enhanced resolution at the sub-nanometer or even at the sub-angstrom level. The emergence of smart photon-avalanche optical materials is gradually shaping the nanoworld.

This review has highlighted the emerging applications of ANPs beyond traditional applications in theranostics and conventional confocal imaging. Through careful selection of dopant ions and their concentration in the host lattice, the emission profile of ANPs can be tuned, providing greater control over emission spectra. The combination of spectral design, NIR excitation, and multiplexing capabilities due to narrow emission bands positions ANPs as powerful tools for super-resolution imaging, *in vivo* biological treatment, and optical data storage. Significant progress has been observed in the forensic arena, where ANPs find usefulness due to the scarcity of lanthanides in the environment and the need for specialized laboratories for their production. ANPs offer superior contrast, sensitivity, selectivity, facile surface modification, and photostability compared with traditional luminescence fluorescent visualization methods. Additionally, the ultimate optical properties of ANPs, such as their giant optical nonlinear response over minute pumping sources, power-dependent emission tuning, and narrow emission spectra, make them suitable tools for driving photochemical reactions, such as reversible photoswitching and bidirectional switching of ligand spin states. As a result, ANPs have considerable potential in the development of novel light-responsive photonic devices, materials, and remote-control probes, as well as advancing spintronics.

The modification of ANPs with optical highlighters and targeting groups has shown promise as a tool for sub-diffraction-

unlimited photomanipulation at plasma membranes. This capability indicates future potential for ANPs in *in situ* bioanalytic investigations, including protein interaction kinetics and evaluation of spatiotemporal organization at the micro- and nanoscale. However, while ANPs show high stability, low toxicity, and efficient energy transfer through CR pathways, their low absorption cross-section remains a challenge for Photothermal Therapy (PTT) or Photodynamic Therapy (PDT) in cancer treatment. An example of a promising material in biomedicine is neodymium ions, which exhibit advantageous properties, including high absorption cross-section area at the NIR-II window and emitting light in the UV-to-NIR-I region. Studies on animals have explored rare-earth-doped nanocrystals, including ANPs, as potential heaters for therapeutic applications.

In conclusion, this review has summarized the state-of-the-art progress in optical manipulation in upconverting nanomaterials and explored their emerging applications. The tunable spectral and lifetime domains of ANPs form a solid foundation for their frontier applications, both in fundamental research and cutting-edge practical uses. ANPs have played a pivotal role in enhancing spatial and lateral resolutions in fluorescence microscopy, and recent progress in ANPs for super-resolution microscopy imaging is expected to further lower resolution limits. Challenges remain in achieving molecular-scale resolution, but efforts to minimize fluorescent probe size and linkage distances offer potential solutions. Additionally, ANPs have demonstrated significant utility in photopolymerization for 3D printing and as a crystal lasing medium for solid-state UV lasers through WGM incorporation. Their unique optical properties make them effective alternatives for super-resolution and deep tissue imaging under the NIR-II window, surpassing traditional NIR-to-visible-based imaging. Furthermore, ANPs engineered to exhibit persistent luminescence properties enable longer nanoparticle tracking. Despite these significant advancements, challenges persist, necessitating further research efforts to overcome fundamental limitations and realize widespread use of ANP-based technologies. Future explorations hold promise for groundbreaking innovations and advancements in diverse scientific and technological domains through the continuous refinement and exploration of ANPs' capabilities.

Data availability

This is a review paper and as such it does not include any primary datasets. All the data we discussed and analyzed within this review are derived from the published studies and literature references in the manuscript.

Conflicts of interest

The authors declare no conflict of interest.

References

1 H. Ni and S. C. Rand, *Opt. Lett.*, 1992, **17**, 1222–1224.
2 C. Lee, E. Z. Xu, Y. Liu, A. Teitelboim, K. Yao, A. Fernandez-Bravo, A. M. Kotulska, S. H. Nam, Y. D. Suh, A. Bednarkiewicz, B. E. Cohen, E. M. Chan and P. J. Schuck, *Nature*, 2021, **589**, 230–235.
3 Y. Liang, Z. Zhu, S. Qiao, X. Guo, R. Pu, H. Tang, H. Liu, H. Dong, T. Peng, L. D. Sun, J. Widengren and Q. Zhan, *Nat. Nanotechnol.*, 2022, **17**, 524–530.
4 C. Lee, E. Z. Xu, K. W. C. Kwock, A. Teitelboim, Y. Liu, H. S. Park, B. Ursprung, M. E. Ziffer, Y. Karube, N. Fardian-Melamed, C. C. S. Pedroso, J. Kim, S. D. Pritzl, S. H. Nam, T. Lohmueller, J. S. Owen, P. Ercius, Y. D. Suh, B. E. Cohen, E. M. Chan and P. J. Schuck, *Nature*, 2023, **618**, 951–958.
5 Z. Korczak, M. Dudek, M. Majak, M. Misiak, L. Marciniak, M. Szalkowski and A. Bednarkiewicz, *Low-Temp. Phys.*, 2023, **49**, 322–329.
6 D. F. Luz, R. F. da Silva, C. V. T. Maciel, G. Soares, E. P. Santos, C. Jacinto, L. J. Q. Maia, B. C. Lima and A. L. Moura, *Appl. Opt.*, 2023, **62**, C30–C37.
7 Y. Shang, J. Zhou, Y. Cai, F. Wang, A. Fernandez-Bravo, C. Yang, L. Jiang and D. Jin, *Nat. Commun.*, 2020, **11**, 6156.
8 A. Skripka, M. Lee, X. Qi, J. A. Pan, H. Yang, C. Lee, P. J. Schuck, B. E. Cohen, D. Jaque and E. M. Chan, *Nano Lett.*, 2023, **23**, 7100–7106.
9 M. Schnermann, *Nature*, 2017, **551**, 176–177.
10 Y. Yang and F. Zhang, *Eur. J. Nucl. Med. Mol. Imaging*, 2022, **49**, 3226–3246.
11 J. Lippincott-Schwartz and G. H. Patterson, *Science*, 2003, **300**, 87–91.
12 P. Van Roessel and A. Brand, *Nat. Cell Biol.*, 2002, **4**, E15–E20.
13 A. P. Demchenko, *Methods Appl. Fluoresc.*, 2020, **8**, 022001.
14 W. Zheng, P. Huang, Z. Gong, T. Datao, X. Jin, Z. Qilin, L. Renfu, Y. Wenwu, G. B. Jean-Claude and C. Xueyuan, *Nat. Commun.*, 2018, **9**, 3462.
15 G. Yang, M. Kazes, D. Raanan and D. Oron, *ACS Photonics*, 2021, **8**, 1909–1916.
16 O. V. Chashchikhin and M. F. Budyka, *J. Photochem. Photobiol., A*, 2017, **343**, 72–76.
17 I. I. Vlasov, A. A. Shiryaev, T. Rendler, S. Steinert, S. Y. Lee, D. Antonov, M. Vörös, F. Jelezko, A. V. Fisenko, L. F. Semjonova, J. Biskupek, U. Kaiser, O. I. Lebedev, I. Sildos, P. R. Hemmer, V. I. Konov, A. Gali and J. Wrachtrup, *Nat. Nanotechnol.*, 2014, **9**, 54–58.
18 R. Gupta, G. H. Darwish and W. R. Algar, *J. Phys. Chem. C*, 2022, **126**, 20960–20974.
19 L. Đorđević, F. Arcudi and M. Prato, *Nat. Protoc.*, 2019, **14**, 2931–2953.
20 M.-H. Chan, B.-G. Chen, L. T. Ngo, W.-T. Huang, C.-H. Li, R.-S. Liu and M. Hsiao, *Pharmaceutics*, 2021, **13**, 1874.
21 D. Ghosh, A. F. Bagley, Y. J. Na, M. J. Birrer, S. N. Bhatia and A. M. Belcher, *Proc. Natl. Acad. Sci. U. S. A.*, 2014, **111**, 13948–13953.

22 N. M. Iverson, P. W. Barone, M. Shandell, L. J. Trudel, S. Sen, F. Sen, V. Ivanov, E. Atolia, E. Farias, T. P. McNicholas, N. Reuel, N. M. Parry, G. N. Wogan and M. S. Strano, *Nat. Nanotechnol.*, 2013, **8**, 873–880.
23 B. Chang, D. Li, Y. Ren, C. Qu, X. Shi, R. Liu, H. Liu, J. Tian, Z. Hu, T. Sun and Z. Cheng, *Nat. Biomed. Eng.*, 2022, **6**, 629–639.
24 K. Du, J. Feng, X. Gao and H. Zhang, *Light: Sci. Appl.*, 2022, **11**, 222.
25 X. Li, Q. Zou, W. Li and C. Haifeng, *Sci. Rep.*, 2018, **8**, 11267.
26 A. Bednarkiewicz, E. M. Chan, A. Kotulska, L. Marciniak and K. Prorok, *Nanoscale Horiz.*, 2019, **4**, 881–889.
27 X. Zhao, Q. Liu, X. Li, H. Li, Z. Shen, H. Ji and T. Ma, *Angew. Chem., Int. Ed.*, 2023, **62**, e202219214.
28 B. Golesorkhi, I. Taarit, H. Bolvin, H. Nozary, J. R. Jiménez, C. Besnard, L. Guénée, A. Fürstenberg and C. Piguet, *Dalton Trans.*, 2021, **50**, 7955–7968.
29 G. Sun, Y. Xie, Y. Wang, H. Zhang and L. Sun, *Angew. Chem., Int. Ed.*, 2023, **62**, e202312308.
30 B. Zhou, B. Tang, C. Zhang, C. Qin, Z. Gu, Y. Ma, T. Zhai and J. Yao, *Nat. Commun.*, 2020, **11**, 1174.
31 M. Xue, X. Zhu, X. Qiu, Y. Gu, W. Feng and F. Li, *ACS Appl. Mater. Interfaces*, 2016, **8**, 17894–17901.
32 G. Sun, Y. Xie, Y. Wang, G. A. Mandl, S. L. Maurizio, H. Zhang and L. Sun, *Angew. Chem., Int. Ed.*, 2023, **62**, e202304591.
33 M.-F. Joubert, *Opt. Mater.*, 1999, **11**, 181–203.
34 M.-F. Joubert, S. Guy, B. Jacquier and C. Linarés, *Opt. Mater.*, 1994, **4**, 43–49.
35 M. Dudek, Z. Korczak, K. Prorok, O. Bezkrovnyi, L. Sun, M. Szalkowski and A. Bednarkiewicz, *Nanoscale*, 2023, **15**, 18613–18623.
36 S. Wen, J. Zhou, K. Zheng, A. Bednarkiewicz, X. Liu and D. Jin, *Nat. Commun.*, 2018, **9**, 2415.
37 E. S. Levy, C. A. Tajon, T. S. Bischof, J. Iafrati, A. Fernandez-Bravo, D. J. Garfield, M. Chamanzar, M. M. Maharbiz, V. S. Sohal, P. J. Schuck, B. E. Cohen and E. M. Chan, *ACS Nano*, 2016, **10**, 8423–8433.
38 J. S. Chivian, W. E. Case and D. D. Eden, *Appl. Phys. Lett.*, 1979, **35**, 124–125.
39 N. J. Krasutsky, *J. Appl. Phys.*, 1983, **54**, 1261–1267.
40 N. Pelletier-Allard and R. Pelletier, *Opt. Commun.*, 1991, **81**, 247–250.
41 F. Auzel, *Chem. Rev.*, 2004, **104**(1), 139–173.
42 W. Lenth and R. M. Macfarlane, *J. Lumin.*, 1990, **45**, 346–350.
43 A. Brenier and A. M. Jurdyc, *J. Lumin.*, 1996, **69**, 131–140.
44 T. Hebert, R. Wannemacher, R. M. MacFarlane and W. Lenth, *Appl. Phys. Lett.*, 1992, **60**, 2592–2594.
45 M. F. Joubert, S. Guy, S. Cuerq and P. A. Tanner, *J. Lumin.*, 1997, **75**, 287–293.
46 D. Wang, Y. Guo, G. Sun, J. Li, L. Zhao and G. Xu, *J. Alloys Compd.*, 2008, **451**, 122–124.
47 H. Ni and S. C. Rand, *Opt. Lett.*, 1991, **16**, 1424–1426.
48 M. Malinowski, A. Wnuk, Z. Frukacz, G. Chadeyron, R. Mahiou, S. Guy and M. F. Joubert, *J. Alloys Compd.*, 2001, **323**, 731–735.
49 M. E. Koch, A. W. Kueny and W. E. Case, *Appl. Phys. Lett.*, 1990, **56**, 1083–1085.
50 B. P. Scott, F. Zhao, R. S. Chang and N. Djeu, *Opt. Lett.*, 1993, **18**, 113–115.
51 B. C. Collings and A. J. Silversmith, *J. Lumin.*, 1994, **62**, 271–279.
52 F. Auzel and Y. Chen, *J. Lumin.*, 1995, **65**, 45–56.
53 V. François, F. Pellé, P. Goldner and D. Simkin, *J. Lumin.*, 1995, **65**, 57–63.
54 J. P. Jouart, M. Bouffard, T. Duvaut and N. M. Khaidukov, *Chem. Phys. Lett.*, 2002, **366**, 62–66.
55 X. Wang, S. Xiao, Y. Bu, X. Yang and J. W. Ding, *Opt. Lett.*, 2008, **33**, 2653–2655.
56 F. Auzel, Y. Chen and D. Meichenin, *J. Lumin.*, 1994, **60–61**, 692–694.
57 I. R. Martin, V. D. Rodriguez, Y. Guyot, S. Guy, G. Boulon and M.-F. Joubert, *J. Phys.: Condens. Matter*, 2000, **12**, 1507–1516.
58 F. Lahoz, I. R. Martín, V. L. Guadalupe, J. Méndez-Ramos, V. D. Rodríguez and U. R. Rodríguez-Mendoza, *Opt. Mater.*, 2004, **25**, 209–213.
59 M. F. Joubert, S. Guy, C. Linares, B. Jacquier and J. L. Adam, *J. Non-Cryst. Solids*, 1995, **184**, 98–102.
60 S. Guy, D. P. Shepherd, M.-F. Joubert, B. Jacquier and H. Poignant, *J. Opt. Soc. Am.*, 1997, **14**, 926–934.
61 P. Stremplewski, C. Koepke and D. Piątkowski, *Appl. Phys. B*, 2012, **107**, 171–176.
62 A. Gomes, G. S. Maciel, R. E. Aratijo, L. Acioli and C. Aratijo, *Opt. Commun.*, 1993, **103**, 361–364.
63 P. Xie and T. R. Gosnell, *Opt. Lett.*, 1995, **20**, 1014.
64 Y. Chen, D. Meichenin and F. E. Auzel, *J. Phys.: Condens. Matter*, 1995, **7**, 3363–3370.
65 G. Liu, Y. H. Chen and J. V. Beitz, *J. Lumin.*, 1999, **81**, 7–12.
66 Y. Chen and F. Auzel, *J. Phys. D: Appl. Phys.*, 1995, **28**, 207–211.
67 V. Lavín, F. Lahoz, I. R. Martín, U. R. Rodríguez-Mendoza and J. M. Cáceres, *Opt. Mater.*, 2005, **27**, 1754–1761.
68 M. Dudek, M. Szalkowski, M. Misiak, M. Ćwierzona, A. Skripka, Z. Korczak, D. Piątkowski, P. Woźniak, R. Lisiecki, P. Goldner, S. Maćkowski, E. M. Chan, P. J. Schuck and A. Bednarkiewicz, *Adv. Opt. Mater.*, 2022, **10**, 2201052.
69 K. W. C. Kwock, C. Lee, A. Teitelboim, Y. Liu, K. Yao, S. B. Alam, B. E. Cohen, E. M. Chan and P. J. Schuck, *J. Phys. Chem. C*, 2021, **125**, 23976–23982.
70 J. Chen and J. X. Zhao, *Sensors*, 2012, **12**, 2414–2435.
71 C. Wang, Z. Wen, R. Pu, B. Pan, B. Wang, K. Zheng, Y. Du and Q. Zhan, *Adv. Mater.*, 2024, **36**, e2307848.
72 C. Wang, Z. Wen, R. Pu and Q. Zhan, *Laser Photonics Rev.*, 2024, **18**, 2400290.
73 H. Wu, B. Pan, Q. Zhao, C. Wang, R. Pu, C. Liu, Z. Chen, Z. Luo, J. Huang, W. Wei, T. Chen and Q. Zhan, *Adv. Photonics*, 2024, **6**, 056010.

74 J. Chen, C. Liu, S. Xi, S. Tan, Q. He, L. Liang and X. Liu, *Res. Sq.*, 2024, preprint (version 1), DOI:DOI: **10.21203/rs.3.rs-4183918/v1**.
75 A. Ivaturi, S. K. W. MacDougall, R. Martin-Rodriguez, M. Quintanilla, J. Marques-Hueso, K. W. Kramer, A. Meijerink and B. S. Richards, *J. Appl. Phys.*, 2013, **114**, 013505.
76 A. Patra, C. S. Friend, R. Kapoor and P. N. Prasad, *Chem. Mater.*, 2003, **15**, 3650–3655.
77 G. Mialon, S. Turkcan, G. Dantelle, D. P. Collins, M. Hadjipanayi, R. A. Taylor, T. Gacoin, A. Alexandrou and J. P. Boilott, *J. Phys. Chem. C*, 2010, **114**, 22449.
78 G. A. Kumar, M. Pokhrel, A. Martinez, R. C. Dennis, I. L. Villegas and D. K. Sardar, *J. Alloys Compd.*, 2012, **513**, 559–565.
79 Y. Li, X. Wei and M. Yin, *J. Alloys Compd.*, 2011, **509**, 9865–9868.
80 G. Chen, H. Qiu, P. N. Prasad and X. Chen, *Chem. Rev.*, 2014, **114**, 5161–5214.
81 Z. Zhang, A. Skripka, J. C. Dahl, C. Dun, J. J. Urban, D. Jaque, P. J. Schuck, B. E. Cohen and E. M. Chan, *Angew. Chem., Int. Ed.*, 2023, **62**, e202212549.
82 M. Zhang, P. Huang, W. Zheng, X. Song, X. Shang, W. Zhang and X. Chen, *Nano Lett.*, 2023, **23**, 8576–8584.
83 A. Skripka, Z. Zhang, X. Qi, B. Ursprung, P. Ercius, B. E. Cohen, P. J. Schuck, D. Jaque and E. M. Chan, arXiv, 2024, preprint, arXiv:2403.04098, DOI:DOI: **10.48550/arXiv.2403.04098**.
84 M. M. Waldrop, *Nature*, 2016, **530**, 144–147.
85 H.-T. Peng, M. A. Nahmias, T. F. De Lima, A. N. Tait and B. J. Shastri, *IEEE J. Sel. Top. Quantum Electron.*, 2018, **24**, 1–15.
86 A. Bednarkiewicz, M. Szalkowski, M. Majak, Z. Korczak, M. Misiak and S. Mackowski, *Adv. Mater.*, 2023, **35**, 2304390.
87 D. A. B. Miller, *Nat. Photonics*, 2010, **4**, 3–5.
88 J.-A. Pan, A. Skripka, C. Lee, X. Qi, A. L. Pham, J. J. Woods, R. J. Abergel, P. J. Schuck, B. E. Cohen and E. M. Chan, *J. Am. Chem. Soc.*, 2024, **146**, 7487–7497.
89 S. W. Hell and J. Wichmann, *Opt. Lett.*, 1994, **19**, 780–782.
90 T. A. Klar and S. W. Hell, *Opt. Lett.*, 1999, **24**, 954–956.
91 T. A. Klar, S. Jakobs, M. Dyba, A. Egner and S. W. Hell, *Proc. Natl. Acad. Sci. U. S. A.*, 2000, **97**, 8206–8210.
92 J. B. Pawley, *Handbook of Biological Confocal Microscopy*, Springer US, 1995.
93 A. Schuldt, *Nat. Rev. Mol. Cell Biol.*, 2010, **11**, 678.
94 G. Vicidomini, P. Bianchini and A. Diaspro, *Nat. Methods*, 2018, **15**, 173–182.
95 R. Pu, Q. Zhan, X. Peng, S. Liu, X. Guo, L. Liang, X. Qin, Z. W. Zhao and X. Liu, *Nat. Commun.*, 2022, **13**, 6636.
96 N. Sun, Y. Jia, S. Bai, Q. Li, L. Dai and J. Li, *Adv. Colloid Interface Sci.*, 2023, **314**, 102880.
97 Y. Hou, M. Laasmaa, J. Li, X. Shen, O. Manfra, E. S. Nordén, C. Le, L. Zhang, I. Sjaastad, P. P. Jones, C. Soeller and W. E. Louch, *Nat. Cardiovasc. Res.*, 2023, **2**, 251–267.
98 V. Bayle, J. B. Fiche, C. Burny, M. P. Platre, M. Nollmann, A. Martiniere and Y. Jaillais, *Nat. Protoc.*, 2021, **16**, 1600–1628.
99 M. Bates, S. A. Jones and X. Zhuang, *Cold Spring Harb. Protoc.*, 2013, **8**, 498–520.
100 Y. Wu and H. Shroff, *Nat. Methods*, 2018, **15**, 1011–1019.
101 M. Lelek, M. T. Gyparaki, G. Beliu, F. Schueder, J. Griffié, S. Manley, R. Jungmann, M. Sauer, M. Lakadamyali and C. Zimmer, *Nat. Rev. Methods Primers*, 2021, **1**, 39.
102 A. N. Butkevich, H. Ta, M. Ratz, S. Stoldt, S. Jakobs, V. N. Belov and S. W. Hell, *ACS Chem. Biol.*, 2018, **13**, 475–480.
103 H. Zhang, M. Zhao, I. M. Ábrahám and F. Zhang, *Front. Bioeng. Biotechnol.*, 2021, **9**, 692075.
104 F. Grimm, S. Nizamov and V. N. Belov, *ChemBioChem*, 2019, **20**, 2248–2254.
105 R. Kasper, B. Harke, C. Forthmann, P. Tinnefeld and S. W. Hell, *Small*, 2010, **6**, 1379–1384.
106 J. Hanne, H. J. Falk, F. Görlitz, P. Hoyer, J. Engelhardt, S. J. Sahl and S. W. Hell, *Nat. Commun.*, 2015, **6**, 1727.
107 Z. Zhu, Y. Liang, Q. Zhao, H. Wu, B. Pan, S. Qiao, B. Wang and Q. Zhan, *Sci. Bull.*, 2024, **69**, 458–465.
108 Y. Liu, Y. Lu, X. Yang, X. Zheng, S. Wen, F. Wang, X. Vidal, J. Zhao, D. Liu, Z. Zhou, C. Ma, J. Zhou, J. A. Piper, P. Xi and D. Jin, *Nature*, 2017, **543**, 229–233.
109 Q. Zhan, H. Liu, B. Wang, Q. Wu, R. Pu, C. Zhou, B. Huang, X. Peng, H. Agreen and S. He, *Nat. Commun.*, 2017, **8**, 1058.
110 Y. Li, R. Wang, W. Zheng and Y. Li, *Inorg. Chem.*, 2019, **58**, 8230–8236.
111 C. Liu, B. Pan, B. Wang, Q. Zhao, Y. Ni, H. Wu, Z. Luo, T. Chen and Q. Zhan, *Optica*, 2024, **11**, 1324–1333.
112 A. Hlavacek, Z. Farka, M. J. Mickert, U. Kostiv, J. C. Brandmeier, D. Horak, P. Skladal, F. Foret and H. H. Gorris, *Nat. Protoc.*, 2022, **17**, 1028–1072.
113 L. Liang, Z. Feng, Q. Zhang, T. D. Cong, Y. Wang, X. Qin, Z. Yi, M. J. Y. Ang, L. Zhou, H. Feng, B. Xing, M. Gu, X. Li and X. Liu, *Nat. Nanotechnol.*, 2021, **16**, 975–980.
114 X. Di, D. Wang, Q. P. Su, Y. Liu, J. Liao, M. Maddahfar, J. Zhou and D. Jin, *Proc. Natl. Acad. Sci. U. S. A.*, 2022, **119**, e2207402119.
115 A. Feuchtinger, A. Walch and M. Dobosz, *Histochem. Cell Biol.*, 2016, **146**, 781–806.
116 G. Pitruzzello, *Nat. Res.*, 2023, **17**, 376–377.
117 H. Deng, S. Huang and C. Xu, *Talanta*, 2018, **184**, 461–467.
118 X. Wu, G. Chen, J. Shen, Z. Li, Y. Zhang and G. Han, *Bioconjugate Chem.*, 2015, **26**, 166–175.
119 G. Xiang, X. Liu, Q. Xia, X. Liu, S. Xu, S. Jiang, X. Zhou, L. Li, D. Wu, L. Ma, X. Wang and J. Zhang, *Talanta*, 2021, **224**, 121832.
120 C. Bradac, S. F. Lim, H. C. Chang and I. Aharonovich, *Adv. Opt. Mater.*, 2020, **8**, 2000183.
121 X. Qiu, Q. Zhou, X. Zhu, Z. Wu, W. Feng and F. Li, *Nat. Commun.*, 2020, **11**, 4.
122 C. D. S. Brites, A. Millán and L. D. Carlos, *Handb. Phys. Chem. Rare Earths*, 2016, **49**, 339–427.

123 A. C. Brandão-Silva, M. A. Gomes, Z. S. Macedo, J. F. M. Avila, J. J. Rodrigues Jr. and M. A. R. C. Alencar, *J. Phys. Chem. C*, 2018, **122**, 20459–20468.
124 S. Balabhadra, M. L. Debasu, C. D. S. Brites, L. A. O. Nunes, O. L. Malta, J. Rocha, M. Bettinelli and L. D. Carlos, *Nanoscale*, 2015, **7**, 17261–17267.
125 A. Benayas, B. Del Rosal, A. Pérez-Delgado, K. Santacruz-Gómez, D. Jaque, G. A. Hirata and F. Vetrone, *Adv. Opt. Mater.*, 2015, **3**, 687–694.
126 D. Wawrzynczyk, A. Bednarkiewicz, M. Nyk, W. Strek and M. Samoc, *Nanoscale*, 2012, **4**, 6959–6961.
127 I. E. Kolesnikov, E. V. Golyeva, M. A. Kurochkin, E. Lähderanta and M. D. Mikhailov, *Sens. Actuators, B*, 2016, **235**, 287–293.
128 R. R. Zairov, A. P. Dovzhenko, S. N. Podyachev, S. N. Sudakova, T. A. Kornev, A. E. Shvedova, A. N. Masliy, V. V. Syakaev, I. S. Alekseev, I. M. Vatsouro, G. S. Mambetova, D. V. Lapaev, I. R. Nizameev, F. Enrichi, A. M. Kuznetsov, V. V. Kovalev and A. R. Mustafina, *Colloids Surf., B*, 2022, **217**, 112664.
129 S. A. Wade, S. F. Collins and G. W. Baxter, *J. Appl. Phys.*, 2003, **94**, 4743–4756.
130 J. Stefańska, A. Bednarkiewicz and L. Marciniak, *J. Mater. Chem. C*, 2022, **10**, 5744–5782.
131 K. Trejgis, K. Ledwa, K. Maciejewska, L. Li and L. Marciniak, *Sci. Rep.*, 2022, **12**, 5847.
132 C. Y. Morassuti, L. A. O. Nunes, S. M. Lima and L. H. C. Andrade, *J. Lumin.*, 2018, **193**, 39–43.
133 A. S. Souza, L. A. Nunes, I. G. Silva, F. A. Oliveira, L. L. da Luz, H. F. Brito, M. C. Felinto, R. A. Ferreira, S. A. Júnior, L. D. Carlos and O. L. Malta, *Nanoscale*, 2016, **8**, 5327–5333.
134 J. Xiong, M. Zhao, X. Han, Z. Cao, X. Wei, Y. Chen, C. Duan and M. Yin, *Sci. Rep.*, 2017, **7**, 41311.
135 L. Marciniak, A. Bednarkiewicz and K. Elzbieciak, *J. Mater. Chem. C*, 2018, **6**, 7568–7575.
136 K. Trejgis, K. Maciejewska, A. Bednarkiewicz and L. Marciniak, *ACS Appl. Nano Mater.*, 2020, **3**, 4818–4825.
137 M. Szalkowski, M. Dudek, Z. Korczak, C. Lee, L. Marciniak, E. M. Chan, P. J. Schuck and A. Bednarkiewicz, *Opt. Mater.: X*, 2021, **12**, 100102.
138 A. Paściak, R. Marin, L. Abiven, A. Pilch-Wróbel, M. Misiak, W. Xu, K. Prorok, O. Bezkrovnyi, L. Marciniak, C. Chanéac, F. Gazeau, R. Bazzi, S. Roux, B. Viana, V. Lehto, D. Jaque and A. Bednarkiewicz, *ACS Appl. Mater. Interfaces*, 2022, **14**, 33555–33566.
139 R. E. Slusher, *Opt. Photonics News*, 1993, **4**, 2.
140 L. He, S. K. Özdemir and L. Yang, *Laser Photonics Rev.*, 2013, **7**, 60–82.
141 P. Miao, Z. Zhang, J. Sun, W. Walasik, S. Longhi, N. M. Litchinitser and L. Feng, *Science*, 2016, **353**, 464–467.
142 L. F. Johnson and H. J. Guggenheim, *Appl. Phys. Lett.*, 1971, **19**, 44–47.
143 Y. Urata, T. Fukuda and S. Wada, in *Advanced Solid-State Lasers C*, 2001, vol. 40, p. 6453.
144 X. Chen, T. Sun and F. Wang, *Chem. – Asian J.*, 2020, **15**, 21–33.
145 E. Castellano-Hernández, M. D. Serrano, R. J. Riobóo, C. Cascales, C. Zaldo, A. Jeżowski and P. Loiko, *Cryst. Growth Des.*, 2016, **16**, 1480–1491.
146 M. Khajavikhan, A. Simic, M. Katz, J. H. Lee, B. Slutsky, A. Mizrahi, V. Lomakin and Y. Fainman, *Nature*, 2012, **482**, 204–207.
147 A. Fernandez-Bravo, D. Wang, E. S. Barnard, A. Teitelboim, C. Tajon, J. Guan, G. C. Schatz, B. E. Cohen, E. M. Chan, P. J. Schuck and T. W. Odom, *Nat. Mater.*, 2019, **18**, 1172–1176.
148 J. Pichaandi, J. C. Boyer, K. R. Delaney and F. C. J. M. van Veggel, *J. Phys. Chem.*, 2011, **115**, 19054–19064.
149 A. Fernandez-Bravo, K. Yao, E. S. Barnard, N. J. Borys, E. S. Levy, B. Tian, C. A. Tajon, L. Moretti, M. V. Altoe, S. Aloni, K. Beketayev, F. Scotognella, B. E. Cohen, E. M. Chan and P. J. Schuck, *Nat. Nanotechnol.*, 2018, **13**, 572–577.
150 Y. Liu, A. Teitelboim, A. Fernandez-Bravo, K. Yao, M. V. P. Altoe, S. Aloni, C. Zhang, B. E. Cohen, P. J. Schuck and E. M. Chan, *ACS Nano*, 2020, **14**, 1508–1519.
151 Y. Lu, J. Zhao, R. Zhang, Y. Liu, D. Liu, E. M. Goldys, X. Yang, P. Xi, A. Sunna, J. Lu, Y. Shi, R. C. Leif, Y. Huo, J. Shen, J. A. Piper, J. P. Robinson and D. Jin, *Nat. Photonics*, 2014, **8**, 32–36.
152 X. Liu, Z. H. Chen, H. Zhang, Y. Fan and F. Zhang, *Angew. Chem., Int. Ed.*, 2021, **60**, 7041–7045.
153 Y. Gu, Z. Guo, W. Yuan, M. Kong, Y. Liu, Y. Liu, Y. Gao, W. Feng, F. Wang, J. Zhou, D. Jin and F. Li, *Nat. Photonics*, 2019, **13**, 525–531.
154 H. Li, M. Tan, X. Wang, F. Li, Y. Zhang, L. L. Zhao, C. Yang and G. Chen, *J. Am. Chem. Soc.*, 2020, **142**, 2023–2030.
155 R. Deng, F. Qin, R. Chen, W. Huang, M. Hong and X. Liu, *Nat. Nanotechnol.*, 2015, **10**, 237–242.
156 A. Bednarkiewicz, M. Szalkowski, M. Majak, Z. Korczak, M. Misiak and S. Maćkowski, *Adv. Mater.*, 2023, **35**, e2304390.
157 V. Emiliani, E. Entcheva, R. Hedrich, P. Hegemann, K. R. Konrad, C. Luscher, M. Mahn, Z.-H. Pan, R. R. Sims, J. Vierock and O. Yizhar, *Nat. Rev. Methods Primers*, 2022, **2**, 55.
158 K. Deisseroth, *Nat. Methods*, 2011, **8**, 26–29.
159 A. Bednarkiewicz, E. M. Chan and K. Prorok, *Nanoscale Adv.*, 2020, **2**, 4863–4872.
160 M. T. Manzari, Y. Shamay, H. Kiguchi, N. Rosen, M. Scaltriti and D. A. Heller, *Nat. Rev. Mater.*, 2021, **6**, 351–370.
161 A. Tewabe, A. Abate, M. Tamrie, A. Seyfu and E. A. Siraj, *J. Multidiscip. Healthcare*, 2021, **14**, 1711–1724.